# Eddy - Internal Wave Interactions: Stimulated Cascades in Cross-scale Kinetic Energy and Enstrophy Fluxes

Roy Barkan, [a,b] Kaushik Srinivasan,[b] and James C. McWilliams [b]

[a] *Porter School of the Environment and Earth Sciences, Tel Aviv University, Tel Aviv, Israel.*

[b] *Department of Atmospheric and Oceanic Sciences, University of California Los Angeles, Los Angeles, CA, USA.*

*Corresponding author*: Roy Barkan, rbarkan@tauex.tau.ac.il

ABSTRACT: The interactions between oceanic mesoscale eddies, submesoscale currents, and internal gravity waves (IWs) are investigated in submesoscale resolving realistic simulations in the North Atlantic Ocean. Using a novel analysis framework that couples the coarse-graining method in space with temporal filtering and a Helmholtz decomposition, we quantify the effects of the interactions on the cross-scale kinetic energy (KE) and enstrophy fluxes. By systematically comparing solutions with and without IW forcing we show that externally-forced IWs stimulate a reduction in the KE inverse cascade associated with mesoscale rotational motions and an enhancement in the KE forward cascade associated with convergent submesoscale currents – i.e., a *stimulated cascade* process. The corresponding IW effects on the enstrophy fluxes are seasonally dependent, with a stimulated reduction (enhancement) in the forward enstrophy cascade during summer (winter). Direct KE and enstrophy transfers from currents to IWs are also found, albeit with weaker magnitudes compared with the *stimulated cascades*. We further find that the forward KE and enstrophy fluxes associated with IW motions are almost entirely driven by scattering of the waves by the rotational eddy field, rather than by wave-wave interactions. This process is investigated in detail in a companion manuscript. Finally, we demonstrate that the *stimulated cascades* are spatially localized in coherent structures. Specifically, the magnitude and direction of the bi-directional KE fluxes at submesoscales are highly correlated with, and inversely proportional to, divergence-dominated circulations, and the inverse KE fluxes at mesoscales are highly correlated with strain dominated circulations. The predominantly forward enstrophy fluxes in both seasons are also correlated with strain dominated flow structures.

## 1. Introduction

Oceanic mesoscale eddies (with spatial scales of $\mathcal{O}$(10-100) km and time scales of $\mathcal{O}$(1) week) are well described by geostrophic turbulence theory (Charney 1971; Salmon 1980) that predicts kinetic energy (KE) transfers to large scales (inverse KE cascade) and enstrophy transfers to smaller scales (forward enstrophy cascade). These so-called *balanced* motions – characterized by small Rossby numbers ($Ro \ll 1$) and large Richardson numbers ($Ri \gg 1$) – contain a large fraction of the oceanic KE reservoir, transfer large amounts of heat across the world oceans, and therefore play an important role in the climate system (Wunsch and Ferrari 2004). The smaller and more rapidly evolving submesoscales currents (spatial scales of $\mathcal{O}$(1-10) km and time scales of $\mathcal{O}$(1) day) are characterized by $Ro \sim Ri \sim \mathcal{O}(1)$ (Thomas et al. 2008; McWilliams 2016), strong ageostrophic circulations, and a negative correlation between the vertical component of vorticity, $\zeta$, and the horizontal divergence, $\delta$ (Capet et al. 2008a; Barkan et al. 2019). They exhibit a dual KE cascade: an inverse cascade associated with mixed-layer eddies and a forward cascade associated with frontogenesis (Capet et al. 2008b; Schubert et al. 2020; Balwada et al. 2022; Garabato et al. 2022; Srinivasan et al. 2023), and are therefore considered to lie in the cusp between balanced an unbalanced motions in the sense that there is no *balanced* model that can accurately capture all of their statistical and phenomenological properties.

Oceanic internal gravity waves (IWs) exhibit a continuous distribution of KE across spatial and temporal scales[1] (e.g., the IW continuum; Garrett and Munk 1972), despite being forced at large spatial scales by atmospheric storms at the inertial frequency (i.e., near-inertial IWs; NIWs), and by the barotropic tide interacting with bathymetric features at diurnal and semi-diurnal frequencies (i.e., internal tides). Traditionally, the formation of the IW continuum is explained by weakly non-linear wave-wave interactions dominated by resonant and near-resonant triads (McComas and Bretherton 1977; Lvov et al. 2012; Eden et al. 2019) that lead to a forward spatial KE cascade and a dual temporal KE cascade.[2]

In recent years, a growing number of theoretical and idealized numerical studies highlighted a number of possible mechanisms for the interactions between IWs and mesoscale eddies (Xie and Vanneste 2015; Taylor and Straub 2016; Wagner and Young 2016; Rocha et al. 2018; Taylor and Straub 2020; Thomas and Daniel 2020); with only a few studies examining interactions

[1] bounded between the Coriolis frequency $f$ and the Brunt-Vaisala frequency $N$.
[2] a forward temporal cascade is generally expected but Parametric Subharmonic Instability can, in theory, lead to an inverse temporal cascade.

with submesoscale currents as well (Thomas 2012; Whitt and Thomas 2015; Barkan et al. 2017). Specifically, it was shown that NIWs can exchange KE with mesoscale quasi-gestrophic currents (Xie and Vanneste 2015; Rocha et al. 2018) and submesoscale fronts and filaments (Whitt and Thomas 2015; Kar and Barkan 2023) – a mechanism we refer to as direct exchanges – and that high-frequency NIWs can modify and catalyze the turbulent KE cascades of lower-frequency mesoscale and submesoscale currents (Barkan et al. 2017; Xie 2020; Thomas and Daniel 2021) – a mechanism we refer to as *stimulated cascades*. In addition, it was demonstrated that mesoscale eddies can scatter and refract IWs, providing a whole new mechanism for the formation of the commonly observed IW continuum (Kafiabad et al. 2019; Dong et al. 2020; Savva et al. 2021; Cox et al. 2023; Dong et al. 2023; Yang et al. 2023). Barkan *et al.* (2021; hereinafter B21) systematically quantified the interactions between mesoscale eddies, submesoscale eddies, and IWs in a suite of realistically forced numerical simulations in the Iceland basin, that were extensively validated with field measurements. Using a coarse-graining framework (Germano 1992; Eyink 2005; Aluie et al. 2018), B21 demonstrated that externally forced IWs significantly reduce the subinertial temporal KE inverse cascades and enhance the sub-to super-inertial forward KE cascades, with the strongest forward fluxes localized in submesoscale fronts and filaments that dynamically depart from geostrophic balance. These findings imply that externally forced IWs can lead to substantial depletion of mesoscale KE, thereby highlighting the important role of the interactions in determining how the ocean will equilibrate in a changing climate.

Here, we extend the work of B21 using a novel analysis framework, and examine in detail how the interactions between mesoscale eddies, submesoscale currents, and IWs (i.e., eddy-wave interactions) modify the spatial cross scale KE fluxes. With geostrophic turbulence theory in mind, we also evaluate how eddy-wave interactions modify the cross-scale enstrophy fluxes, focusing more generally on the effects IWs have on the cross-scale transfers associated with turbulent eddying motions , i.e., on the *stimulated cascades* mechanism. In a companion paper (Delpech et al. 2023) we test the generality of our findings by analyzing eddy-wave interactions in the California Current System, with an emphasis on the mechanisms leading to the formation of the IW continuum.

The manuscript is organized as follows: in Section 2 we describe the setup of our numerical simulations; in Sections 3 and 4 we describe the new framework used to quantify eddy-wave interaction effects on the cross-scale KE and enstrophy cascades; in Section 5 we compare the KE and enstrophy fluxes between solutions with and without externally forced IWs; in Section 6 we quantify the spatial locality of the interactions; and in Section 7 we summarize and discuss our findings.

## 2. Model Setup

Numerical simulations are carried out using the Regional Oceanic Modeling System (ROMS; Shchepetkin and McWilliams 2005) forced by the Climate Forecast System Reanalysis (CFSR) atmospheric product (Dee et al. 2014), with gradual nesting to zoom in on the Iceland Basin (Fig. 1). This region has complex current-topography interactions (Fratantoni 2001), a rich mesoscale eddy field (Jakobsen et al. 2003), strong NIW activity (Chaigneau et al. 2008), and was the target location for the Near-Inertial Shear and Kinetic Energy in the North Atlantic experiment (Thomas et al. 2020, 2023).

The analysis is based on two simulation sets with 2 km and 500 m horizontal grid spacing. The first set (hereinafter *hf* ) is forced by hourly winds, hourly boundary conditions from a parent 6 km solution (not shown), and includes TPXO-based (Egbert et al. 1994; Egbert and Erofeeva 2002) barotropic tidal forcing at the boundary. The second set (hereinafter *sm* ) has no tidal forcing, and the high frequency component of the wind forcing and boundary conditions are removed, using a low-pass filter with a one-day width, to eliminate IWs. Both simulation sets are run for a full year, but we focus our analysis on winter months (January, February, March) and summer months (July, August, September), using hourly output fields.

Additional details about the numerical setup are provided in B21, where it was demonstrated that the solutions presented here agree well with altimetry based measurements of geostrophic eddy kinetic energy, with Argo-based measurements of stratification, and with mooring based measurements of kinetic energy power spectral densities (up to frequencies of approximately 1/5 $\mathrm{hr}^{-1}$).

## 3. Coarse grained kinetic energy and enstropy fluxes

B21 demonstrated that the IW field in the *hf* solutions substantially modifies the temporal cross-scale energy cascades, reducing the magnitude of the inverse cascade and enhancing the magnitude of the forward cascade compared with the *sm* solutions. Here we augment the analysis of B21 and investigate the spatial cross-scale energy and enstrophy cascades

$$\Pi(\boldsymbol{x},t,\ell) = -T^{\ell}_{ij}\frac{\partial \overline{u_i}^{\ell}}{\partial x_j}, \qquad T^{\ell}_{ij} = \left(\overline{u_i u_j}^{\ell} - \overline{u_i}^{\ell}\,\overline{u_j}^{\ell}\right), \tag{1}$$

$$\Pi_{\zeta}(\boldsymbol{x},t,\ell) = -\mathcal{Z}^{\ell}_{j}\frac{\partial \overline{\zeta}^{\ell}}{\partial x_j}, \qquad \mathcal{Z}^{\ell}_{j} = \left(\overline{u_j \zeta}^{\ell} - \overline{u_j}^{\ell}\,\overline{\zeta}^{\ell}\right), \tag{2}$$

following the coarse-graining framework (Germano 1992; Eyink 2005; Aluie et al. 2018). Above, $\overline{()}^{\ell}$ denotes the width of an isotropic two dimensional low-passed top-hat (i.e., uniform) filter applied to the three dimensional velocity field $(u_1,u_2,u_3) = (u,v,w)$, or the vorticity $\zeta = \partial_x v - \partial_y u$; $\boldsymbol{x} = (x_1,x_2,x_3) = (x,y,z)$ is the three dimensional position vector; $i = 1,2$; $j = 1-3$; and summation over repeated indices is assumed. By systematically varying $\ell$ above we obtain the spatial KE or enstrophy fluxes as a function of filter width, where positive (negative) values indicate a forward (inverse) energy or enstrophy transfer across a scale $\ell$. In what follows, we will often interpret the positive (negative) fluxes across a range of scales as forward (inverse) 'cascades', although they seldom remain constant, as is required for a 'Kolgmogorv' turbulent cascade.[3]

Because top-hat filters are not spectrally sharp, the effective spectral wavelength has been shown to be $\lambda \approx 2.4\ell$ (Srinivasan et al. 2023). Nevertheless, as will be demonstrated explicitly in Section 6, the choice of spatially localized filters proves to be superior because the cross-scale KE and enstrophy fluxes are found to be spectrally non-local. Therefore, in what follows, $\Pi$ and $\Pi_{\zeta}$ are plotted as a function of the equivalent wavenumber $1/\ell \approx 2.4/\lambda$. In some cases, we horizontally average and vertically integrate $\Pi(\boldsymbol{x},t,\ell)$ and $\Pi_{\zeta}(\boldsymbol{x},t,\ell)$ over the domain, as well as over the course of a season, to provide information solely as function of $\ell$ (e.g., Fig. 2). Alternatively, when the depth information is also of interest, we only apply a horizontal and seasonal average (e.g., Fig. 4,c-f). Finally, when we investigate the structural coherence of the cross-scale fluxes, we select specific filter widths, and representative model snapshots and depth levels, to provide spatial information of $\Pi(\boldsymbol{x},t,\ell)$ and $\Pi_{\zeta}(\boldsymbol{x},t,\ell)$ (e.g., Fig. 11).

The complete coarse-grained KE evolution equations are provided in Eyink (2005) and Barkan et al. (2017), and we derive the coarse-grained enstrophy evolution equations in Appendix A. A scale by scale balance analysis of these equations is left for future work and we solely focus here

[3] it is also likely that KE and enstrophy are locally injected in the 'cascading' scale-range.

on $\Pi$ and $\Pi_\zeta$. Furthermore, although the investigation of cross-scale ensrotphy fluxes is motivated by quasigeostrophic turbulence (e.g., Salmon 1980), we emphasize that the horizontal enstrophy in our solutions (i.e., $(u_z^2+v_z^2)/2$) is non-negligible, particularly during winter when submesoscale currents are most active. An extension of the framework described here and in Section 4 to investigate cross-scale horizontal enstrophy fluxes is trivial, although the interpretation of such analysis is most likely quite complex.

### *a. Total fluxes in the hf and sm solutions*

The shape of the depth integrated and horizontally- and seasonally-averaged $\Pi$ in all solutions shows that there are scale ranges with both inverse and forward KE cascades (Fig. 2a,b). Consistent with the temporal-scale flux results of B21, $\Pi$ in the *hf* solutions shows a reduction in the inverse cascades and an enhancement in the forward cascades in both seasons, compared with the *sm* solutions (black vs. blue lines in Fig. 2a,b). The effects of increasing model resolution are substantially more pronounced in winter (solid vs. dashed lines), when submesoscale currents are expected to be most energetic (Callies et al. 2015), implying that the surface intensified ageostrophic frontal and filament circulations play an important role in the transfers. Indeed, $\Pi_\zeta$ is an order of magnitude larger in winter than in summer (Fig. 2c,d), and is showing an enhancement in the forward enstrophy flux in the *hf* solutions, particularly at the finer resolution (solid lines).

Breaking up $\Pi$ into the horizontal ($\Pi_H$; $j = 1,2$ in Eq. 1 ) and vertical ($\Pi_V$; $j = 3$ in Eq. 1) contributions shows that $\Pi_V$ is substantially stronger in the *hf* solutions during both seasons (Figs. 3, 4), with a forward KE cascade at relatively large spatial scales that is strongest near the base of the seasonally-averaged mixed-layer (Figs. 3e, 4e). As shown in B21, in this region the summer pyconcline (associated with the maximum stratificaiton) is shallow ($\approx$50 m deep) and is only slightly deeper than the averaged mixed-layer depth ($\approx$30 m). In winter the stratification is quite weak throughout the water column with $\approx$300-400 m deep thermocline and $\approx$100 m deep mixed-layer, which is why $\Pi_V$ is more vertically spread out than in summer.

Similar to the temporal cascades shown in B21, $\Pi_H$ is strongest in the mixed-layer in winter, with stronger forward cascade magnitudes and somewhat weaker inverse cascade magnitudes in the *hf* solutions (Fig. 4c,d). The reduction in the inverse cascade magnitudes of $\Pi_H$ in the *hf* solutions is substantially more pronounced during summer (Fig. 3a-d). In this season the transfers extend deeper below the mixed-layer base and the forward cascade is nearly absent (Fig. 3c,d).

The vertical enstrophy transfers ($\Pi_{\zeta_V}$; $j = 3$ in Eq. 2) are much weaker than the horizontal ones ($\Pi_{\zeta_H}$; $j = 1,2$ in Eq. 2) for both *hf* and *sm* solutions, during winter and summer (Fig. 5). Similar to the KE cascades, $\Pi_{\zeta_H}$ is concentrated in the mixed-layer during winter and shows significantly stronger magnitudes in the *hf* solution. During summer, the ensrophy fluxes are much weaker than in winter, with a less pronounced difference between *hf* and *sm* solutions (at least when the total fields are considered; see Section 5a).

## 4. Eddy-wave decomposition

Figures 2-5 demonstrate the significant effects externally forced IWs have on the spatial cross-scale KE and enstrophy fluxes in the *hf* solutions. Next, we investigate the various interactions between IWs and eddying motions that dominate the fluxes, to identify the physical mechanisms responsible for the computed cascades. To this end, we decompose the velocity field $u_i$ into the temporal-low passed 'eddy' component $u_i^E$ and the temporal-high passed 'wave' component $u_i^W$, using sixth order Butterworth filters. The resulting coarse-grained KE and enstrophy fluxes (Eqs. 1 and 2) become

$$\Pi(\boldsymbol{x},t,\ell) = \Pi^{\mathrm{eeE}} + \Pi^{\mathrm{wwW}} + \Pi^{\mathrm{wwE}} + \underbrace{\left(\Pi^{\mathrm{ewW}} + \Pi^{\mathrm{weW}}\right)}_{\Pi^{\mathrm{scatt}}} + \underbrace{\left(\Pi^{\mathrm{ewE}} + \Pi^{\mathrm{weE}} + \Pi^{\mathrm{eeW}}\right)}_{\Pi^{\mathrm{res}}}, \tag{3}$$

$$\Pi_\zeta(\boldsymbol{x},t,\ell) = \Pi_\zeta^{\mathrm{eeE}} + \Pi_\zeta^{\mathrm{wwW}} + \Pi_\zeta^{\mathrm{wwE}} + \underbrace{\left(\Pi_\zeta^{\mathrm{ewW}} + \Pi_\zeta^{\mathrm{weW}}\right)}_{\Pi_\zeta^{\mathrm{scatt}}} + \underbrace{\left(\Pi_\zeta^{\mathrm{ewE}} + \Pi_\zeta^{\mathrm{weE}} + \Pi_\zeta^{\mathrm{eeW}}\right)}_{\Pi_\zeta^{\mathrm{res}}}, \tag{4}$$

where the two lower-case letters denote the decomposed eddy or wave velocities comprising the fluctuation stresses $T_{ij}^\ell$ and $Z_j^\ell$, and the upper-case letters denote the eddy or wave velocities comprising $\frac{\partial \overline{u_i}^\ell}{\partial x_j}$ and $\frac{\partial \overline{\zeta}^\ell}{\partial x_j}$. For example, $\Pi^{\mathrm{weW}} = -T_{ij}^{\ell,\mathrm{we}} \frac{\partial \overline{u_i^W}^\ell}{\partial x_j}$, with $T_{ij}^{\ell,\mathrm{we}} = \left(\overline{u_i^w u_j^e}^\ell - \overline{u_i^w}^\ell\, \overline{u_j^e}^\ell\right)$, and similarly for the other terms. Note that $T_{ij}^{\ell,\mathrm{we}} \neq T_{ij}^{\ell,\mathrm{ew}}$ and $Z_j^{\ell,\mathrm{we}} \neq Z_j^{\ell,\mathrm{ew}}$ , which is why there is a total of eight terms in Eqs. (3) and (4). This notation is chosen to highlight that $\frac{\partial \overline{u_i}^\ell}{\partial x_j}$ and $\frac{\partial \overline{\zeta}^\ell}{\partial x_j}$ are associated with scales larger than $\ell$, while $T_{ij}^\ell$ and $Z_j^\ell$ are associated with scales smaller than $\ell$.

We interpret the various flux terms in Eqs. 3 and 4 as 'triad' interactions even though, strictly speaking, they are different from the traditional Kolmogrov-Kraichnan definition of triads that relies on wavenumbers in spectral space. With this in mind, we associate the triads $\Pi^{\mathrm{eeE}}, \Pi_{\zeta}^{\mathrm{eeE}}$ and $\Pi^{\mathrm{wwW}}, \Pi_{\zeta}^{\mathrm{wwW}}$ with cross-scale KE and enstrophy transfers due to eddy-eddy-eddy and wave-wave-wave interactions, respectively. The triads $\Pi^{\mathrm{wwE}}, \Pi_{\zeta}^{\mathrm{wwE}}$, if positive, denote direct extraction of eddy KE or enstrophy by IWs (e.g., Xie and Vanneste 2015; Barkan et al. 2017; Rocha et al. 2018) or spontaneous emission (Vanneste 2013), although this latter process is typically weak for oceanic flows. If negative, these triads can represent rectification of waves into larger scale eddies (e.g., Zhang and Xie 2023; Delpech et al. 2023). The triads $\Pi^{\mathrm{scatt}}, \Pi_{\zeta}^{\mathrm{scatt}}$ in Eqs. (3, 4) denote cross-scale fluxes where the eddying motions act as a catalyst for wave-wave transfers. They resemble the IW scattering mechanism discussed in Savva et al. (2021), which is how we will refer to them hereinafter. Similarly, the triads $\Pi^{\mathrm{ewE}} + \Pi^{\mathrm{weE}}$ and $\Pi_{\zeta}^{\mathrm{ewE}} + \Pi_{\zeta}^{\mathrm{weE}}$ denote eddy KE and enstrophy scattering by IW motions and, finally, the triads $\Pi^{\mathrm{eeW}} + \Pi_{\zeta}^{\mathrm{eeW}}$ denote the transfers from large scale wave KE and enstrophy to small scale eddy KE and enstrophy due to, for example, IW breaking. In effect, these last three triads (denoted by $\Pi_{\mathrm{res}}$, $\Pi_{\mathrm{res}}^{\zeta}$ in Eqs. 3 4) are found to be orders of magnitude weaker in the analysis that follows, and will not be shown nor discussed in detail. A similar decomposition, interpretation, and analysis of these triads using spectral fluxes is provided in Shaham and Barkan (2023).

## *a. Helmholtz decomposition*

The horizontal low-passed velocity field comprising the eddy motions is further decomposed into the rotational and divergent components viz.

$$u = \phi_x + \psi_y, \tag{5}$$

$$v = \phi_y - \psi_x, \tag{6}$$

where $\phi$ is the velocity potential, $\psi$ is a streamfunction, and subscripts denote derivatives. This allows us to isolate the coarse-grained fluxes due to purely rotational flow components, which largely represent balanced motions, from the ones that include horizontally divergent flows, representative of frontal ageostrophic circulations (Capet et al. 2008a; D'Asaro et al. 2018; Barkan et al. 2019;

Srinivasan et al. 2023; Kar and Barkan 2023). In the Helmholtz decomposition above we solve for the divergent velocity, assuming it vanishes at the computational boundaries, and the rotational velocity is computed as the difference between the total and divergent velocity components.[4]

For linear internal waves the ratio between the divergent to the rotational velocity components is proportional to $\omega/f$, where $\omega$ is the IW intrinsic frequency and $f$ the Coriolis frequency (e.g., Shaham and Barkan 2023). We therefore expect higher frequency IWs to be predominantly divergent. However, in our high-latitude study region (Fig. 1) semidiurnal internal tides and even higher frequency IWs have non-negligible rotational components and we therefore do not further decompose the high-passed IW velocity field. We emphasize that in lower-latitudes such a decomposition into rotational and divergent flow components may prove insightful in identifying the dominant IW motions responsible for the cross-scale energy and enstrophy fluxes.

### *b. Sensitivity to the choice of filter width*

The Eulerian-based temporal filtering methodology outlined above to separate eddy and IW motions can be inaccurate for a number of reasons. First, Doppler shifting and IW refraction (particularly for NIWs) can lead to wave periods longer than the local inertial period (of $\sim$ 14 hours), as was discussed in Whitt and Thomas (2013), Shakespeare et al. (2021), and Rama et al. (2022). Furthermore, rapid submesoscale frontogenesis events (Barkan et al. 2019) and the sweeping of submesoscale fronts and filaments by lower frequency mesoscale circulations (Callies et al. 2020) can result in non-wave motions with time scales shorter than the inertial period, particularly during winter.

The sensitivity of our analysis to the choice of low-pass and high-pass cutoff periods is demonstrated in Fig. 6 for the *hf* 500 m solution in winter, when the overlap between wave and submesoscale current temporal scales is largest. The horizontal eddy-eddy-eddy KE fluxes ($\Pi_H^{\mathrm{eeE}}$; solid lines in Fig. 6a) show a strong inverse cascade over a wide range of scales, irrespective of the low-pass cutoff period, but the magnitude of the cascades is much stronger when shorter cutoff periods are used. This is because rapid submesoscale mixed-layer eddies are expected to have an inverse cascade (Fox-Kemper et al. 2008; Capet et al. 2008b; Schubert et al. 2020; Srinivasan et al. 2023), which is underestimated for the larger filter widths. Purely rotational $\Pi_H^{\mathrm{eeE}}$ fluxes (dashed lines in Fig. 6a) have a stronger inverse cascade and no forward cascade, demonstrating

[4] for a discussion on the accuracy of this approach, see Srinivasan et al. (2023).

the important role of ageostrophic frontogenetic processes in inducing forward KE fluxes (Capet et al. 2008b; Barkan et al. 2021; Srinivasan et al. 2023). These positive KE fluxes at smaller spatial scales for $\Pi_H^{\mathrm{eeE}}$ (Fig. 6a) and at larger spatial scales for $\Pi_V^{\mathrm{eeE}}$ (Fig. 6b) quantitatively depend on the filter cutoff periods, and we cannot exactly determine whether they are due to eddy-eddy-eddy or wave-wave-wave interactions (Fig. 6, panels a,b vs. c,d). Yang et al. (2023) compared Eulerian and Lagrangian frequency spectra in similar numerical simulations to those presented here and found that IW Doppler shifting is negligible in this region whereas submesosclae sweeping effects can be significant. It is therefore not implausible that some of the forward $\Pi^{\mathrm{wwW}}$ fluxes are associated with submesoscale eddy motions, although their magnitudes are generally much smaller than of the $\Pi^{\mathrm{eeE}}$ fluxes, as will be discussed in Section 5.

With the above caveats in mind, and after extensive experimentation with different filter widths (not shown), we decided to pick 18 hours ($\sim 0.8f$) as the high-passed filter cutoff defining wave motions, and 48 hours as the low-passed filter cutoff defining eddy motions. These cutoff choices allow us to account for rapid eddy motions and for IW refraction, which can be substantial during winter when strongly baroclinic fronts and filaments are present, while still maintaining temporal scale separation to ensure filter leakiness does not affect our results. Evidently, this procedure neglects the cross-scale fluxes that are associated with 18-48 hour velocity periods. We verified that the relative magnitudes of the four dominant triads we discuss are largely insensitive to the neglected fluxes (not shown). Most importantly, it is through careful comparison between the *hf* and *sm* solutions that we can unambiguously quantify the effects IW-eddy interactions have on KE and ensrophy cascades, as will be shown below.

Finally, it is noteworthy that the spatial top-hat filters we use to quantify the cross-scale spatial fluxes cannot adequately resolve the smaller scales (Srinivasan et al. 2023), and that the magnitudes of the positive $\Pi_H^{\mathrm{eeE}}$ fluxes are underestimated (solid black and blue lines in Fig. 6a).[5] This is because top-hat filters are spectrally non-local and so the notion of a 'spectral wavelength' is somewhat fuzzy (e.g., Aluie et al. 2018). We elaborate on the spatial locality of the cascades in section 6.

[5] see Shaham and Barkan (2023) for a similar analysis based on spectral-fluxes.

## 5. Eddy-wave interactions comparison between *hf* and *sm* solutions

Next, we compare the KE and enstrophy fluxes between the *hf* and *sm* solutions, focusing on the four most dominant triads: eeE, wwW, wwE and *scatt* (Eqs. 3 and 4). We distinguish between summer, when the eddy field comprises largely of mesoscale rotational motions, and winter, when the eddy field also includes divergent submesoscale fronts and filaments.

### *a. Summer: mesoscale-IW interactions*

In summer, $\Pi^{\mathrm{eeE}}$ exhibits a clear inverse KE cascade with a magnitude that is insensitive to the choice of low-pass filter cutoff and that peaks at $\ell = \lambda/2.4 \approx 50$ km (solid, dashed, and dot-dashed lines in Fig. 7a). This is consistent with an inverse cascade of slow mesoscale motions, as expected from geostrophic turbulence theory. Accordingly, $\Pi_\zeta^{\mathrm{eeE}}$ exhibits a forward enstrophy cascade that peaks at a smaller scale of $\ell = \lambda/2.4 \approx 5$ km (Fig. 8a)). Remarkably, the inverse KE cascade magnitude reduces substantially in the *hf* solution due to the presence of an energetic IW field (black vs. blue lines in Fig. 7a). This significant reduction in the mesoscale eddy inverse cascade due to the externally forced wave field is one of the major results of this study, and we refer to this mechanism as *stimulated cascades*. This is consistent with the findings of Barkan et al. (2017), B21, Shaham and Barkan (2023), and the companion paper Delpech et al. (2023). Interestingly, this reduction in the *hf* $\Pi^{\mathrm{eeE}}$ inverse cascade is also accompanied by a reduction in the *hf* forward $\Pi_\zeta^{\mathrm{eeE}}$ cascade, although this enstrophy cascade reduction is relatively smaller in magnitude (black vs. blue lines in Fig. 8a)). Some direct KE extraction of mesoscale KE by IWs is also present in the *hf* solution ($\Pi^{\mathrm{wwE}}$; black vs. blue lines in Fig. 7c), although this process is weaker in its effect on the mesoscale KE than is the *stimulated cascade*, and has hardly any enstrophy signal (Fig. 8c).

Most of the forward cascade in the summer *hf* solution is, in fact, explained by the IW scattering mechanism ($\Pi^{\mathrm{scatt}}$; Fig. 7d) with surprisingly little contributions from wave-wave-wave interactions ($\Pi^{\mathrm{wwW}}; Fig.7d$). This scattering dominance of the forward KE cascade is also apparent in $\Pi_\zeta^{\mathrm{scatt}}$ Fig. 8d), because the IW field at this latitude has a non-negligible enstrophy content (Table 1). As expected, IW scattering in summer is entirely because of the rotational eddy field (red circles in Fig. 7d), which accounts for nearly all of the eddy KE in this season (not shown).

*b. Winter: mesoscale-submesoscale-IW interactions*

In winter, as the mixed-layer deepens, mixed-layer instabilities and frontogenesis are ubiquitous in this region leading to the formation of ageostrophic submesoscale circulations and a strong departure from quasigeostrophic dynamics (B21 and Srinivasan et al. 2023). As a result, the eddy field is no longer purely rotational and a forward KE cascade is observed (Fig. 6a). Because submesoscale circulations evolve much more rapidly than mesoscale circulations, $\Pi^{\mathrm{eeE}}$ is substantially more sensitive to the choice of low-pass filter cutoff (solid, dashed, and dot-dashed lines in Fig. 9a). At large spatial scale ($\ell = \lambda/2.4 \gtrapprox 30$ km) and/or long periods (longer than 72 hours) the reduction in the inverse cascade in the *hf* solution is significant (black vs. blue lines in Fig. 9a), similar to that observed in summer. At intermediate spatial and temporal scales (5 km $\lessapprox \ell \lessapprox$ 25 km; 48 to 72 hours), however, the inverse cascade in the *hf* solution is in fact enhanced. This is because the high-frequency wind component in the *hf* solution leads, on average, to a deeper mixed-layer than in the *sm* solution ($\sim$ 120 m compared with $\sim$ 80 m; B21). In turn, some of the excess available potential energy associated with this deeper mixed layer is released to form mixed-layer eddies that undergo an inverse energy cascade (as discussed in Schubert et al. 2020; Srinivasan et al. 2023). Nevertheless, because the magnitude of this enhancement in inverse cascade is smaller than the reduction at large scales; because there is a substantial enhancement in the forward cascade in the *hf* solution at small spatial and temporal scales ($\ell \lessapprox 4$ km; 14 to 48 hours); and because direct extraction is also comparatively positive in the *hf* solution (Fig. 9c), these IW driven processes still lead to the depletion of mesoscale KE, as discussed in B21 (see also Table 1). In contrast with summer, the forward enstrophy cascade in winter is enhanced in the *hf* solution (black vs. blue lines in Fig. 10a). This is potentially because the deeper averaged mixed layer leads to more intense submesoscale frontogenesis that is expected to drive enstrophy further to smaller scales (Barkan et al. 2019; Srinivasan et al. 2023); a process that is entirely missing in (quasi) geostrophic turbulence.

Similar to summer, the forward cascade of IW KE is still dominated by scattering compared with wave-wave-wave interactions (Fig. 9b,d). This is another major result of this study, that is discussed in detail in a companion paper (Delpech et al. 2023). We note here that IW scattering is still largely due to rotational eddy motions, although there is some contributions by non-rotational eddy circulations at small spatial scales (red circles in Fig. 9d ). Furthermore, IW scattering is the most dominant process responsible for the forward enstrophy cascade in the *hf* solution (Fig. 10).

## 6. Spatial locality of the cascades

So far we presented spatially and temporally averaged KE and enstrophy fluxes as a function of an equivalent wavenumber $1/\ell = \lambda/2.4$, where $\lambda$ denotes a spectral wavelength. As discussed in Section 4, the two-dimensional top-hat filters we use for filtering are not spectrally sharp and the conversion between $\ell$ and $\lambda$ is only approximate. As a result, the smallest spectral wavelengths are only marginally resolved by our filtering procedure (i.e., solid black vs. blue lines in Fig. 6). The significance of spectral locality relies on the traditional assumption that cross-scale KE and enstrophy fluxes in turbulent flows are spectrally local (and hence spatially non-local). Because the coarse-graining approach retains spatial information, we can evaluate these traditional assumptions.

To this end we compute the spatial correlations between the horizontal KE and enstrophy fluxes and standard dynamical quantities: the vorticity $\zeta$, the horizontal divergence $\delta$, and the strain rate $S = 1/4\sqrt{(u_x - v_y)^2 + (v_x + u_y)^2}$ (Tables 2 and 3). For illustration purposes we focus on the *hf* $\Pi_H^{\text{eeE}}$ in winter across $\ell = 3$ km, where a forward cascade is found (Fig. 9a), and on the *hf* $\Pi_H^{\text{eeE}}$ in summer across $\ell = 18$ km, where an inverse cascade is found (Fig. 7a). For the enstrophy fluxes we focus on the *hf* $\Pi_{\zeta_H}^{\text{eeE}}$ across $\ell = 3$ km and 5 km in winter and summer, respectively, corresponding to the peak forward enstrophy cascades (Figs. 10a and 8a).

Remarkably, the horizontal coarse-grained KE fluxes in winter at $\ell = 3$ km correlate extremely well with $\delta$ (Table 2 and Fig. 11a,b) with a negative correlation coefficient of $\approx -0.9$. This is consistent with the submesoscale asymptotic regime discussed in Barkan et al. (2019) and Srinivasan et al. (2023); the latter particularly showed that

$$\Pi_H^{\text{eeE}}(\boldsymbol{x}, t, \ell) = (\gamma \overline{S}^{\ell} - \overline{\delta}^{\ell})\mathcal{E}', \tag{7}$$

$$\sim -2\overline{\delta}^{\ell}\mathcal{E}', \tag{8}$$

where $\gamma = (T_{22}^{\ell} - T_{11}^{\ell})/(T_{11}^{\ell} + T_{22}^{\ell})$ is the coordinate dependent stress anisotropy, $\mathcal{E}' = (T_{11}^{\ell} + T_{22}^{\ell})/2$ is the KE at scales smaller than $\ell$, and the simplification in Eq. (8) is valid for anisotropic submesoscale structure with $Ro \sim O(1)$. This explains why convergent (divergent) flows correlate well with a forward (inverse) KE fluxe at a scale of $\ell = 3$ km. Indeed, these submesoscale KE fluxes are spatially localized in frontal and filament regions (Fig. 11a) with the forward transfers also highly correlated with cyclonic regions (Fig. 11c). This agrees with the findings of Barkan et al. (2019) and B21, who demonstrated the high spatial correlation between cyclonic and convergent regions at submesoscale fronts and filaments. In summer, the $\Pi_H^{\mathrm{eeE}}$ inverse cascade across $\ell = 18$ km is also spatially localized (Fig. 12a) and most highly correlated with strain dominated regions (Fig. 12d; Table 2). In this case the flow is predominantly rotational ($\overline{\delta}^{\ell} \to 0$), implying that $\Pi_H^{\mathrm{eeE}} \sim \overline{S}^{\ell}$ (Eq. 7).

The enstrophy fluxes $\Pi_{\zeta_H}^{\mathrm{eeE}}$ are also most correlated with strain dominated regions, particularly during summer (Table 3 and Fig. 13). This spatial locality of cross-scale enstrophy fluxes is perhaps anticipated from two-dimensional turbulence theory (Weiss 1991; Hua et al. 1998) but, to our knowledge, this is the first demonstration of it in realistic ocean simulations.

## 7. Summary and discussion

A plethora of recent theoretical and idealized numerical studies have argued that oceanic mesoscale eddies, submesoscale currents, and IWs can strongly interact, modify the spatiotemporal distribution of KE, and contribute to the depletion of the mesoscale eddy KE reservoir. In this study we test the applicability of these earlier studies in realistic, high-resolution simulations in the north Atlantic Ocean, focusing on the Iceland basin. These simulations have been favorably validated with field measurements (Barkan et al. 2021), and should therefore provide a reasonable quantitative account for the regional oceanic processes at play.

We examine and compare two solution sets at submesoscale permitting (2 km grid spacing) and submesoscale-resolving (500 m grid spacing) resolutions: an *hf* set comprising of both currents, internal tides, and NIWs; and a *sm* set where internal tides and NIWs are explicitly suppressed. We separately analyze summer months, when the mixed-layer is shallow and the currents are dominated by purely rotational deep mesoscale motions, and winter months, when the available potential energy stored in the deeper mixed layer energizes surface-intensified submesoscale eddies, fronts, and filaments with considerable ageostrophic and divergent circulations.

Using the coarse-graining approach, augmented by a temporal decomposition between the slower mesoscale and submesoscale currents and the faster IW motions and also a Helmholtz decomposition, we identify the most dominant triads responsible for KE and enstrophy fluxes across horizontal spatial scales, and evaluate the role of eddy-IW interactions. Although our approach for separating eddies and IWs is quite simple, more elaborate methodologies (e.g., Shakespeare et al. 2021; Torres et al. 2022; Wang et al. 2023)[6] can be trivially implemented in our proposed framework.

We demonstrate that externally forced IWs substantially reduce the inverse KE cascades of slow (time-scales longer that 72 hours) mesoscale motions during both seasons. In summer this reduction in inverse mesoscale KE cascade is accompanied by a reduction in the forward enstorphy cascade. During winter we also observe an IW-induced enhancement in the forward cascade of the more rapidly evolving submesoscale currents (time scales between 14 and 48 hours), potentially because of stronger frontogenesis, as is suggested by an increase in the forward eddy enstrophy cascade in the *hf* solution. These IW-induced modifications to the turbulent eddy cascades – previously coined *stimulated cascades*– are the main proccess responsible for mesoscale KE depletion in this region, with direct KE exchanges a secondary mechanism.

IW KE and enstrophy undergo forward cascades that are dominated by scattering triads rather than by wave-wave-wave triads, as is traditionally assumed. A detailed report of the scattering mechanism, with a careful distinction between NIWs and internal tides, is provided in a companion manuscript (Delpech et al. 2023) that finds qualitatively similar results in the California Current System. We note here that the scattering is dominated by rotational (mesoscale) currents, with some contribution from divergent (submesoscale) currents in winter.

We further demonstrate that the cross-scale KE and enstrophy fluxes are spatially localized in strain- and divergence-dominated coherent structures, emphasizing the advantage of the coarse-graining approach in studying cross-scale transfers in turbulent flows and implying that the transfers are not spectrally-local as is commonly assumed. This suggests that the frequently used characterization of oceanic phenomena based on their spectral wave-lengths can be quite misleading and that future attempts to measure KE and enstrophy fluxes *in situ* should focus on coherent flow structures.

Our analysis suggests that the flow of energy and enstrophy among mesoscale, submesoscale, and IW currents is strong but complicated, as well as somewhat variable with circumstances. But it implies that these are strongly coupled phenomena in many if not most oceanic situations. This

[6]the Wang et al. (2023) decomposition is, in fact, closely related to our approach in that it combines a Helmholtz decomposition with cutoff time scales.

perspective highlights the limits of trying to investigate and interpret their evolutionary behaviors in isolation, as well as to be able to identify unique mechanisms for their interactions. The theories of geophysical fluid dynamics are built upon the interplay between reduced models and computationally simulated or measured reality. We have to acknowledge how challenging this approach is for the oceanic eddy-wave problem.

Current state-of-the-art climate models do not simulate oceanic internal waves and their effects are very crudely parametrized by enhanced diffusivities (e.g., MacKinnon et al. 2017, and refrences therein). If the cross-scale transfer mechanisms presented here are at least qualitatively consistent with those in other ocean basins, then future effort should be directed to improving the representation of eddy-IW interactions in climate models. We argue that these interactions will crucially determine the oceanic equilibrated climate state.

| | winter | | | | summer | | | |
|---|---|---|---|---|---|---|---|---|
| | KE [$\times 10^{-2}\,\mathrm{m}^2/\mathrm{s}^2$] | | enstrophy [$\times 10^{-10}\,1/\mathrm{s}^2$] | | KE [$\times 10^{-2}\,\mathrm{m}^2/\mathrm{s}^2$] | | enstrophy [$\times 10^{-10}\,1/\mathrm{s}^2$] | |
| | *hf* | *sm* | *hf* | *sm* | *hf* | *sm* | *hf* | *sm* |
| Eddy | 1.97 | 2.43 | 5.04 | 3.92 | 1.38 | 1.76 | 1.30 | 1.67 |
| Wave | 0.19 | 0.037 | 4.82 | 2.11 | 0.01 | 0.00**2** | 0.30 | 0.11 |

TABLE 1. The volume- and time-averaged KE and enstrophy associated with the eddy and wave fields during winter and summer, for solutions with (*hf*) and without (*sm*) IW forcing. The eddy field in both season is defined using a sixth order low-passed Butterworth filter with a 48 hour filter width. The wave field in both season is defined using a sixth order high-passed Butterworth filter with an 18 hour filter width. Based on the 500 m solutions.

| | correlation in winter | | | correlation in summer | | |
|---|---|---|---|---|---|---|
| sign of $\Pi_H^{eeE}$ | $\overline{\delta}^{3,14}$ | $\overline{S}^{3,14}$ | $\overline{\zeta}^{3,14}$ | $\overline{\delta}^{18,72}$ | $\overline{S}^{18,72}$ | $\overline{\zeta}^{18,72}$ |
| positive | -0.90 | 0.57 | 0.87 | -0.81 | 0.55 | 0.52 |
| negative | -0.95 | -0.80 | 0.26 | -0.63 | -0.76 | 0.12 |

TABLE 2. Spatially and time averaged correlation coefficients, computed at 2 m depth, between $\Pi_H^{eeE}$ and $\delta$, $S$, and $\zeta$. During winter (summer) the eddy field comprising $\Pi_H^{eeE}$ is computed with 14 hour (72 hour) low-passed fields and fluxes are computed across $\ell = 3$ km ($\ell = 18$ km). The corresponding $\delta$, $S$, and $\zeta$ fields are spatially and temporally low-passed accordingly. Motivated by the Okubo-Weiss parameter (Okubo 1970; Weiss 1991), the vorticity field used to compute the correlation coefficients excludes regions where $\zeta^2 < S^2$. Similarly, the strain field used to compute the correlation coefficients excludes regions where $S^2 < \zeta^2$. The computed correlation coefficients also exclude regions where $|\zeta/f|, S/f, |\delta/f| < 0.1(0.01)$ for winter (summer), and where $\Pi_H^{eeE}$ is smaller than its mean, in both seasons. These various thresholds are used to ensure that the reported correlations are not large because of numerically small values. Refer to Figs. 11 and 12 for visual impression of the spatial structures associated with these correlations. Based on the 500 m solutions.

| | correlation in winter | | | correlation in summer | | |
|---|---|---|---|---|---|---|
| sign of $\Pi^{eeE}_{\zeta_H}$ | $\overline{\delta}^{3,14}$ | $\overline{S}^{3,14}$ | $\overline{\zeta}^{3,14}$ | $\overline{\delta}^{5,72}$ | $\overline{S}^{5,72}$ | $\overline{\zeta}^{5,72}$ |
| positive | -0.62 | 0.68 | 0.61 | -0.40 | 0.76 | 0.37 |
| negative | -0.38 | -0.67 | -0.34 | -0.21 | -0.72 | -0.26 |

TABLE 3. Same as Table 2 for $\Pi^{eeE}_{\zeta_H}$. Note that the enstrophy fluxes in summer are computed across $\ell = 5$ km and so regions where $S/f, |\delta/f|, |\zeta/f < 0.07$ are excluded from the computation of the correlation coefficients during this season. Refer to Fig. 13 for visual impressions of the spatial structures associated with these correlations.

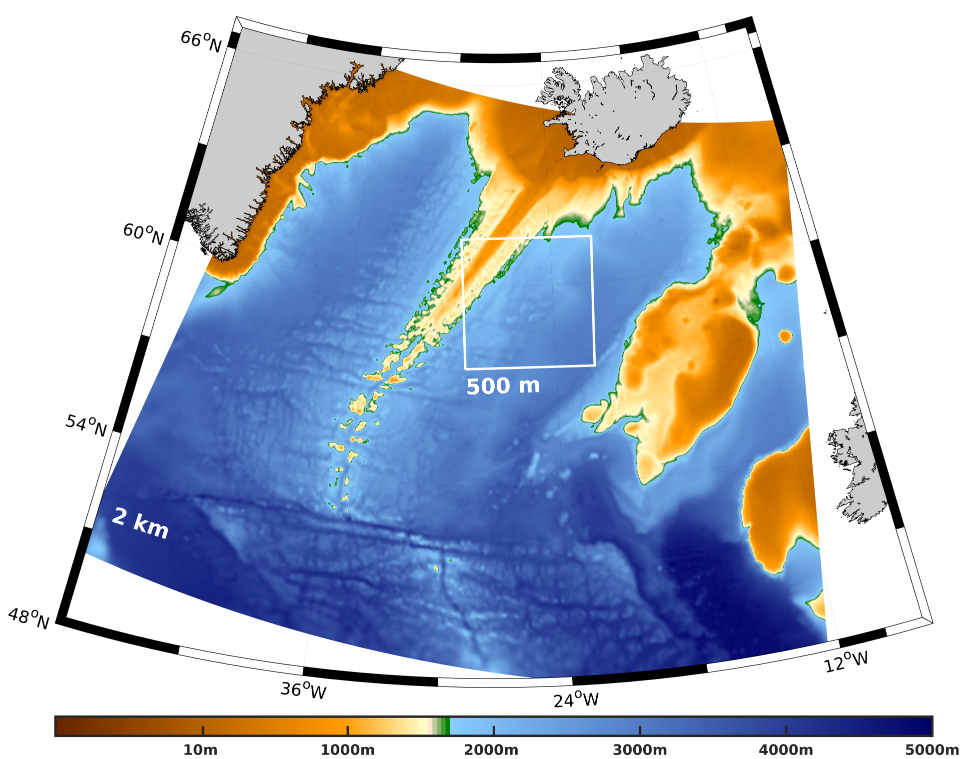


FIG. 1. The ROMS grids used in this study (2 km and 500 m horizontal grid spacings) with colors showing bathymetry.

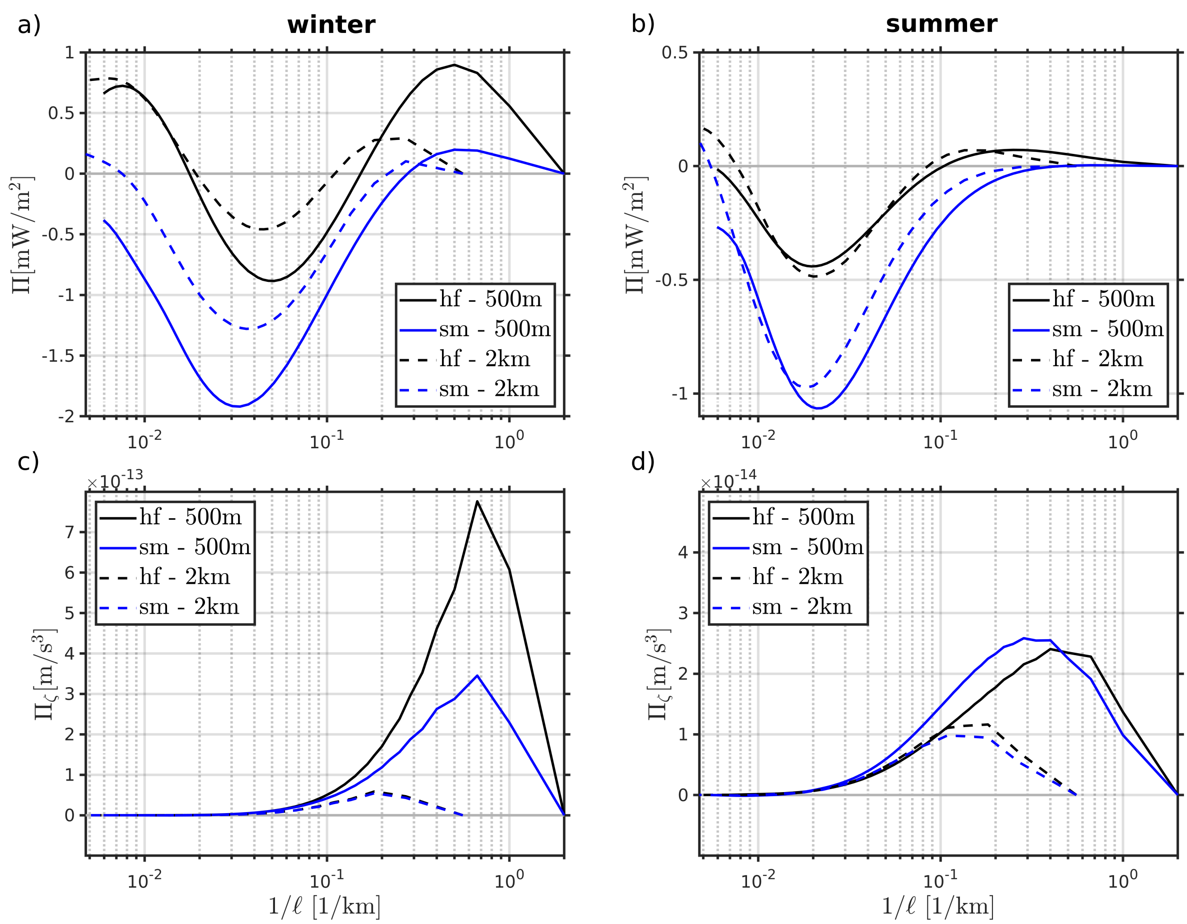


FIG. 2. Depth integrated (over the top 300 m) and seasonally and horizontally averaged (a,b) coarse-grained kinetic energy fluxes, $\Pi$ (Eq. 1), and (c,d) coarse-grained enstrophy fluxes, $\Pi_\zeta$ (Eq. 2), computed for solutions with 2 km (dashed lines) and 500 m (solid lines) grid spacing. *hf* and *sm* denote solutions with and without IW forcing, respectively. Note the differences in the ordinate range between winter (panels a,b) and summer (panels c,d).

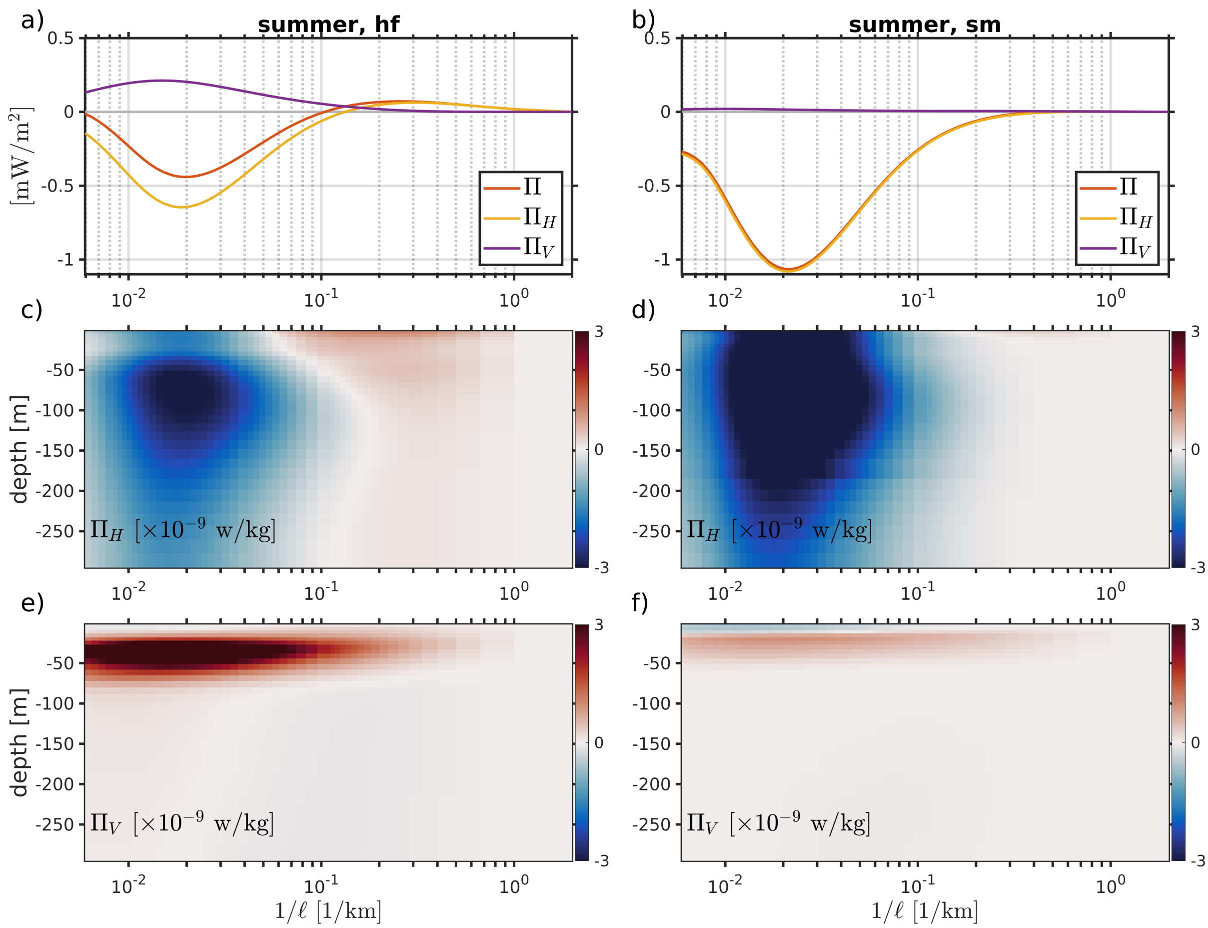


447 Fig. 3. (a,b) Depth integrated (over the top 300 m) and seasonally and horizontally averaged coarse-grained kinetic energy fluxes, $\Pi$ (red lines), along with the contributions from horizontal fluxes ($\Pi_H$; yellow lines) and vertical fluxes ($\Pi_V$; purple lines), for solutions with 500 m grid spacings. (c-f) The corresponding depth structure of the seasonally and horizontally averaged $\Pi_H$ and $\Pi_V$ fluxes. All quantities are computed during summer for solutions with (*hf* ; panels a,c,e) and without (*sm* ; panels b,d,f) IW forcing.

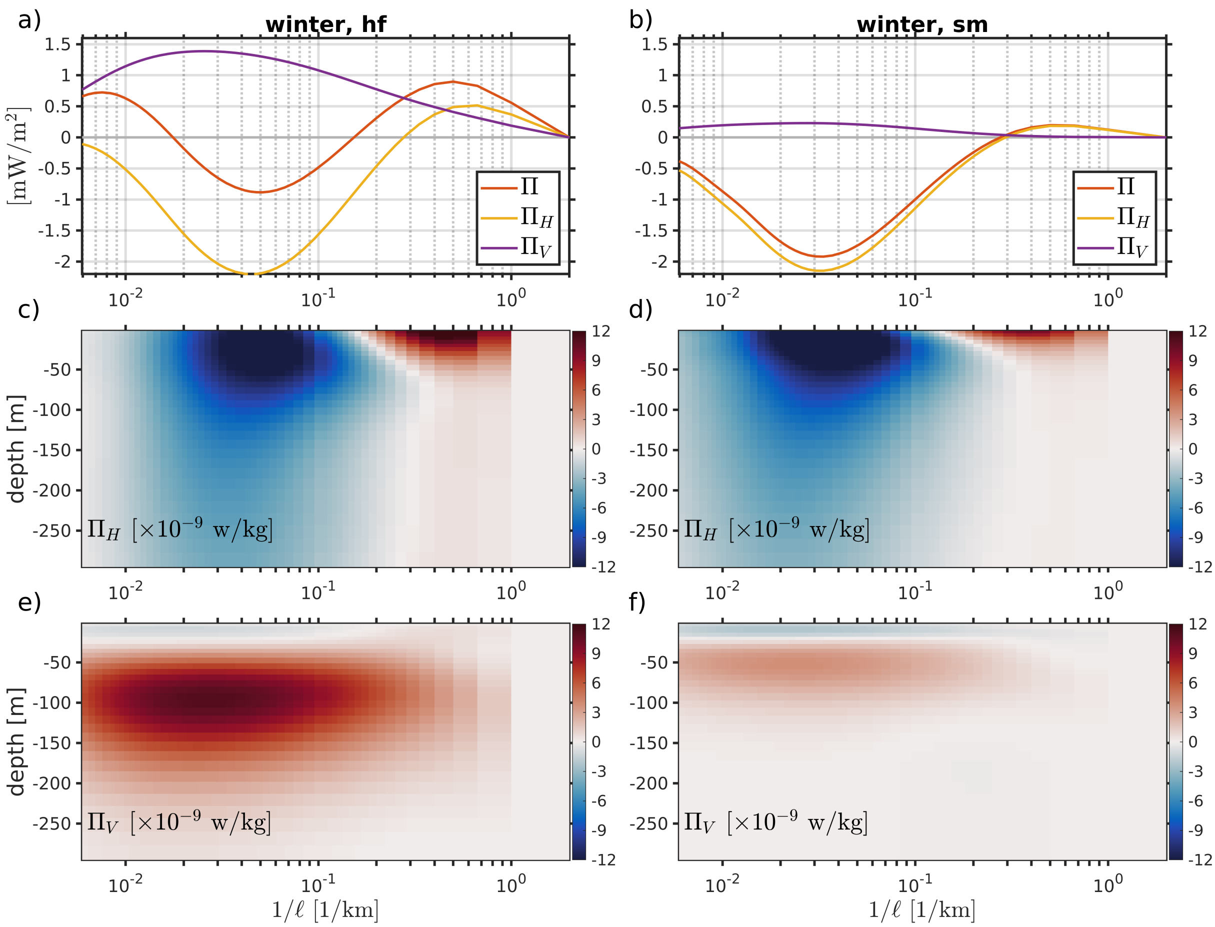


FIG. 4. Same as Fig. 3, during winter. Note the different colorbar ranges compared with summer.

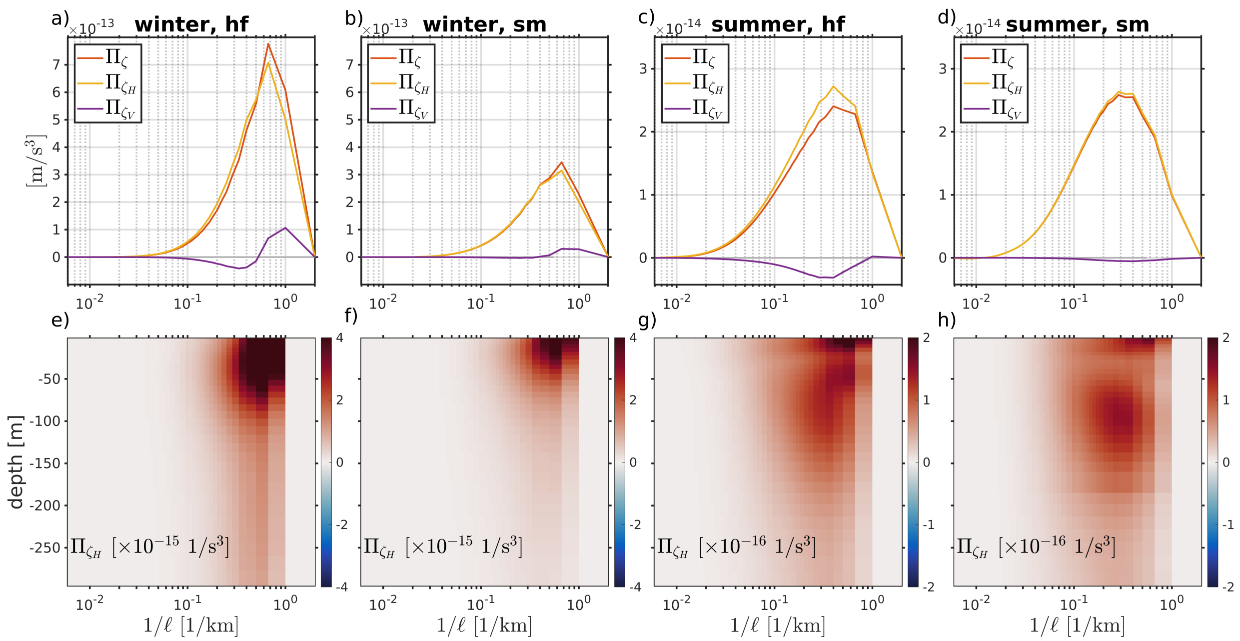


FIG. 5. (a-d) Depth integrated (over the top 300 m) and seasonally and horizontally averaged coarse-grained enstrophy fluxes, $\Pi_\zeta$ (red lines), along with the contributions from horizontal fluxes ($\Pi_{\zeta_H}$; yellow lines) and vertical fluxes ($\Pi_{\zeta_V}$; purple lines), for solutions with 500 m grid spacings. (e-h) The corresponding depth structure of the seasonally and horizontally averaged $\Pi_{\zeta_H}$ fluxes ($\Pi_{\zeta_V}$ fluxes are much weaker; not shown). Note the different ordinate and colorbar ranges between winter (panels a,b,e,f) and summer (panels c,d,g,h) seasons. *hf* and *sm* denote solutions with and without IW forcing, respectively.

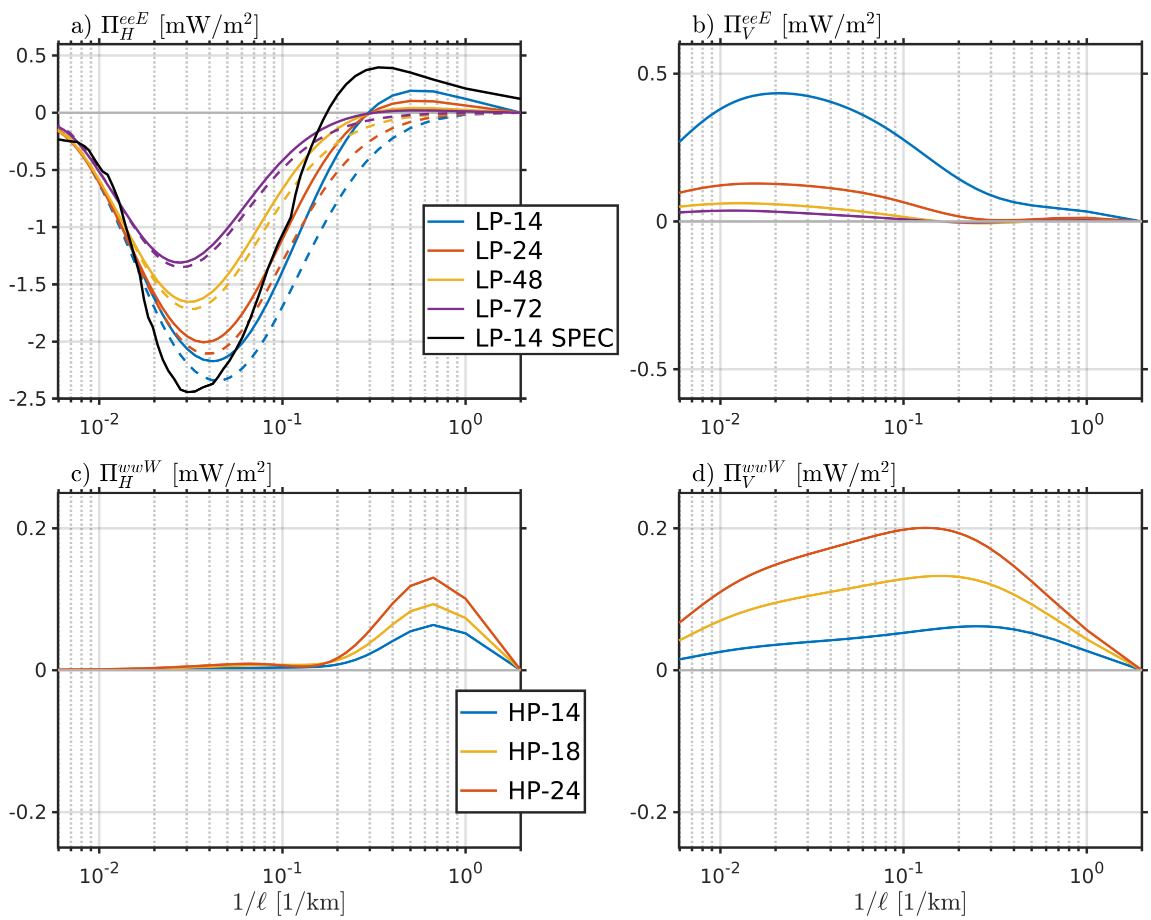


FIG. 6. Depth integrated (over the top 300 m), and seasonally and horizontally averaged, coarse-grained kinetic energy horizontal and vertical fluxes due to eddy motions only ($\Pi^{eeE}$; a,b), and due to wave motions only ($\Pi^{wwW}$; c,d). Different line colors denote the different low-pass (LP) and high-pass (HP) filter widths (in hours) used to separate eddy and wave motions, respectively. Dashed lines in panel a) denote horizontal coarse-grained kinetic energy fluxes due to purely rotational flow components, and the solid black line denotes horizontal coarse-grained kinetic energy fluxes computed using spatial spectral filters. Based on *hf* - 500m solution during winter.

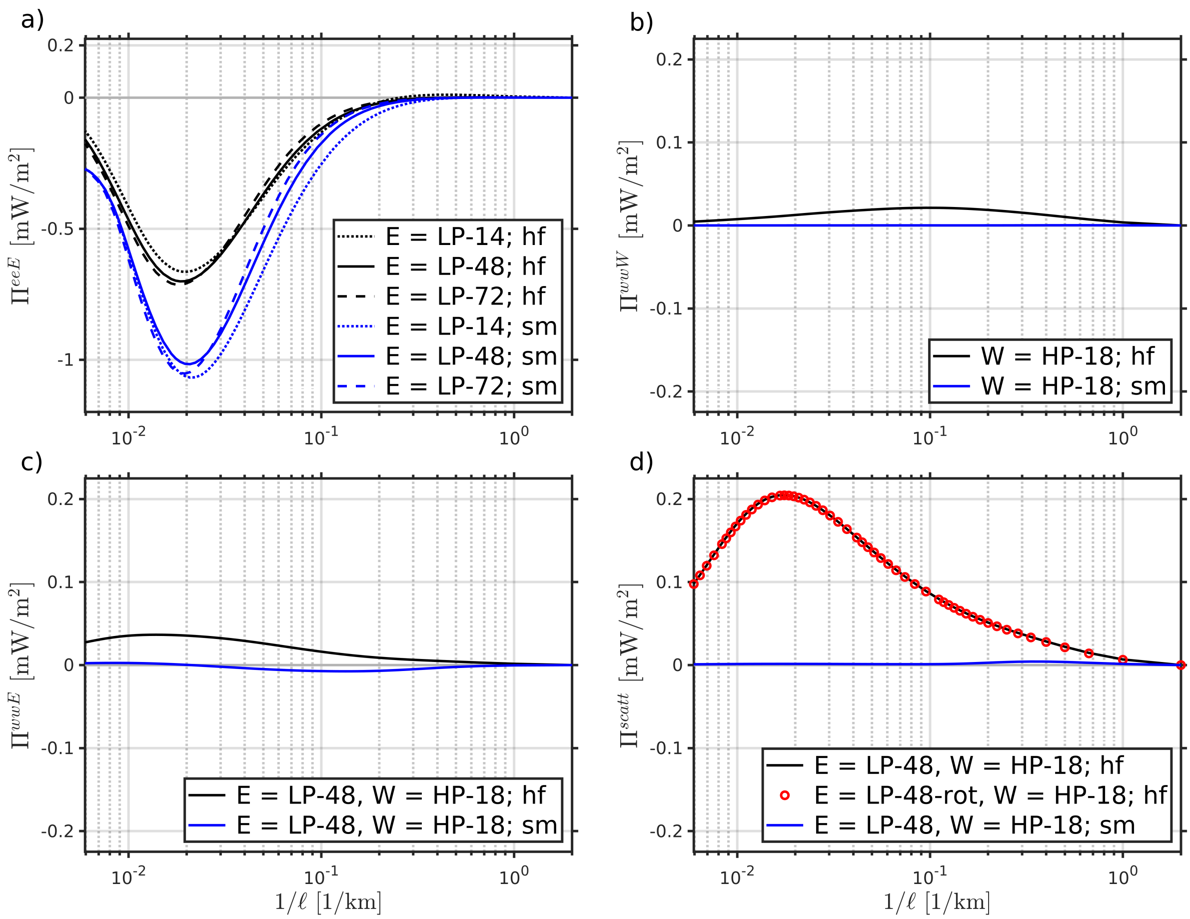


FIG. 7. The four most dominant depth-integrated (over the top 300 m), and seasonally and horizontally averaged, coarse-grained KE triads in Eq. 3, with black and blue lines denoting solutions with (*hf*) and without (*sm*) IW forcing, respectively. E = LP-48 in panels a), c) and d) signifies that the eddy field used in the corresponding triads is computed using a sixth order Butterworth low-passed (LP) filter with a 48 hour filter width. W = HP-18 in panels b,c and d signifies that the wave field used in the corresponding triads is computed using a sixth order Butterworth high-passed (HP) filter with an 18 hour filter width. The different line styles in panel a) denote the different low-pass (LP) filter widths used to compute the eddy field. Red dots in panel d) denote the scattering triad computed with only the rotational low-passed eddy field (LP-48-rot). Based on 500 m solutions during summer.

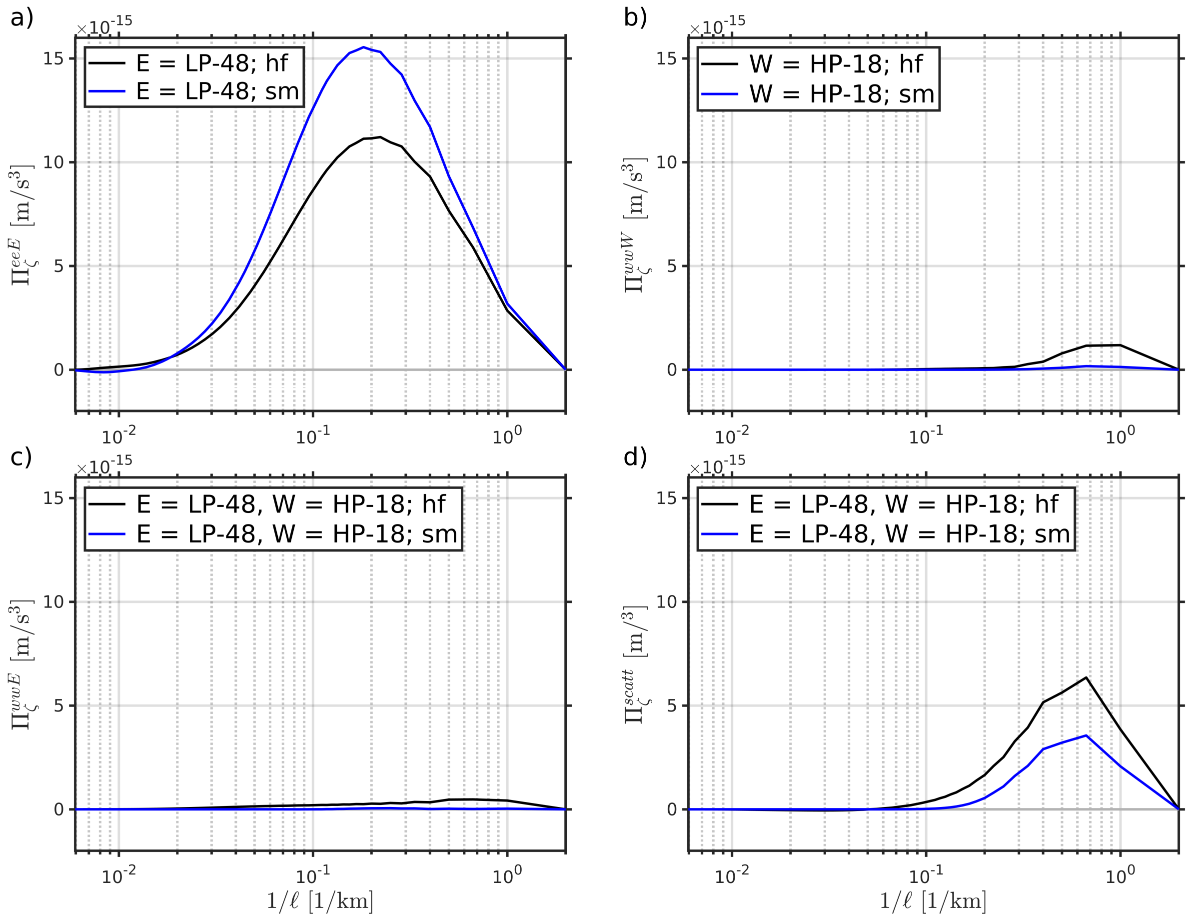


FIG. 8. The four most dominant depth-integrated (over the top 300 m), and seasonally and horizontally averaged, coarse-grained enstrophy triads in Eq. 4, with black and blue lines denoting solutions with (*hf*) and without (*sm*) IW forcing, respectively. The abbreviations and notation are explained in Fig. 7. Based on 500 m solutions during summer.

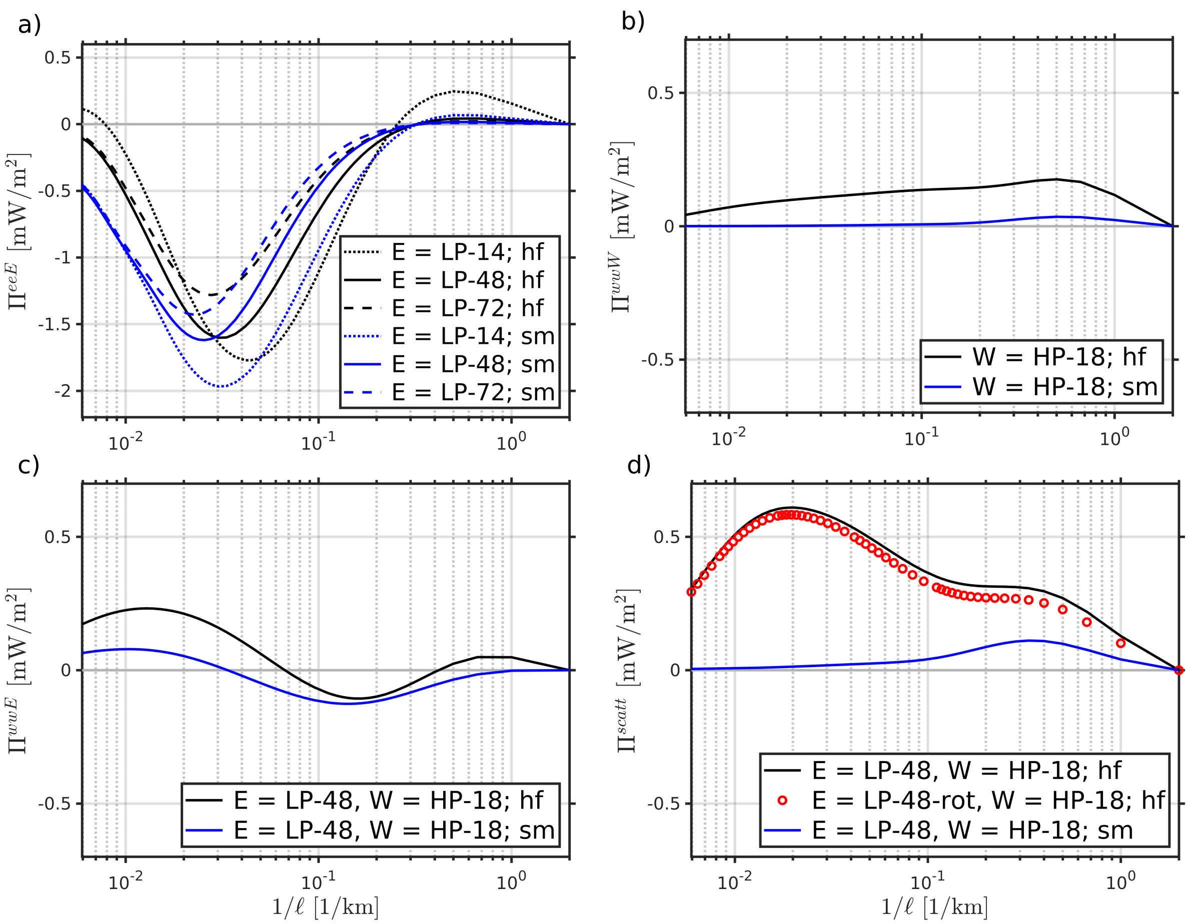


478 Fig. 9. Same as Fig. 7, based on 500 m winter solutions. Note that the ordinate range is extended compared
479 with summer.

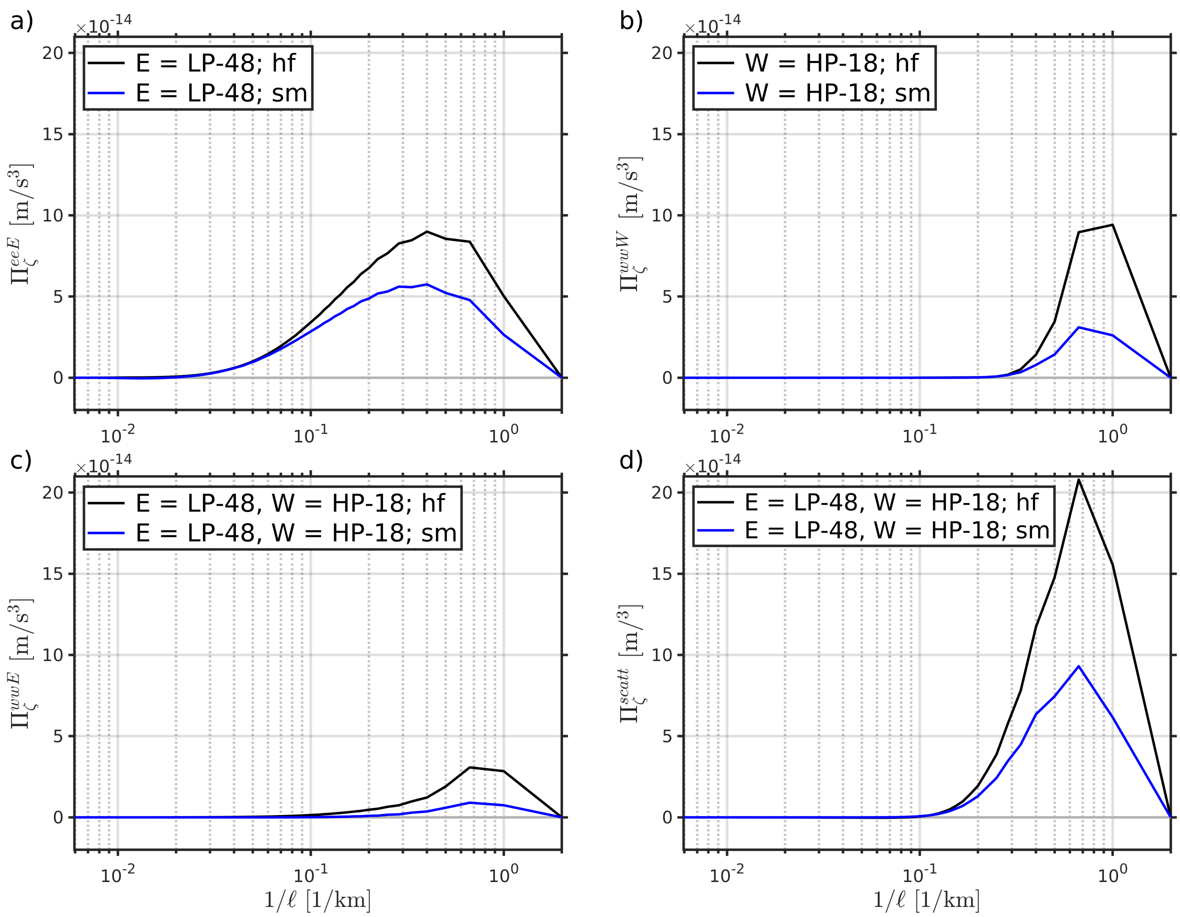


FIG. 10. Same as Fig. 8, based on on 500 m solutions during winter. Note that the ordinate scale is an order of magnitude larger compared with summer. The abbreviations and notation are explained in Fig. 7.

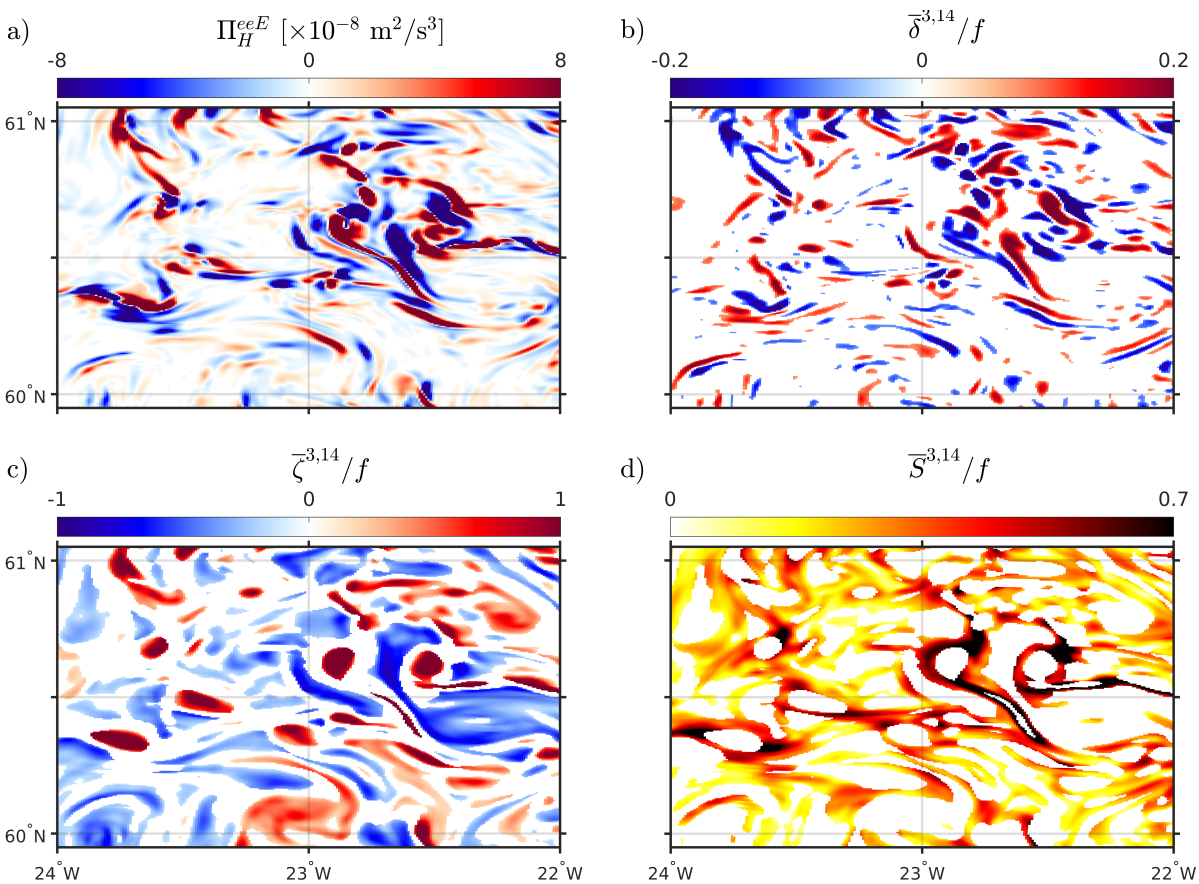


FIG. 11. Representative snapshots of a) horizontal cross-scale KE fluxes and b-d) dynamical flow fields during winter, computed at 2 m depth. The eddy field comprising $\Pi_H^{eeE}$ (panel a) is computed with 14 hour low-passed fields and fluxes are computed across $\ell = \lambda/2.4 = 3$km. The corresponding $\delta/f$ (panel b), $\zeta/f$ (panel c), and $S/f$ (panel d) fields are spatially and temporally low-passed accordingly; e.g., $\overline{\delta}^{3,14}$ denotes the 14 hour temporally low-passed and 3 km spatially low-passed horizontal divergence field. The vorticity field is only plotted where $\zeta^2 > S^2$ and the strain field is only plotted where $S^2 > \zeta^2$. $\Pi_H^{eeE}$ is only plotted where it is larger than the mean and $\delta/f$, $\zeta/f$, and $S/f$ are only plotted where they are larger than 0.1. The corresponding correlation coefficients are displayed in Table 2.

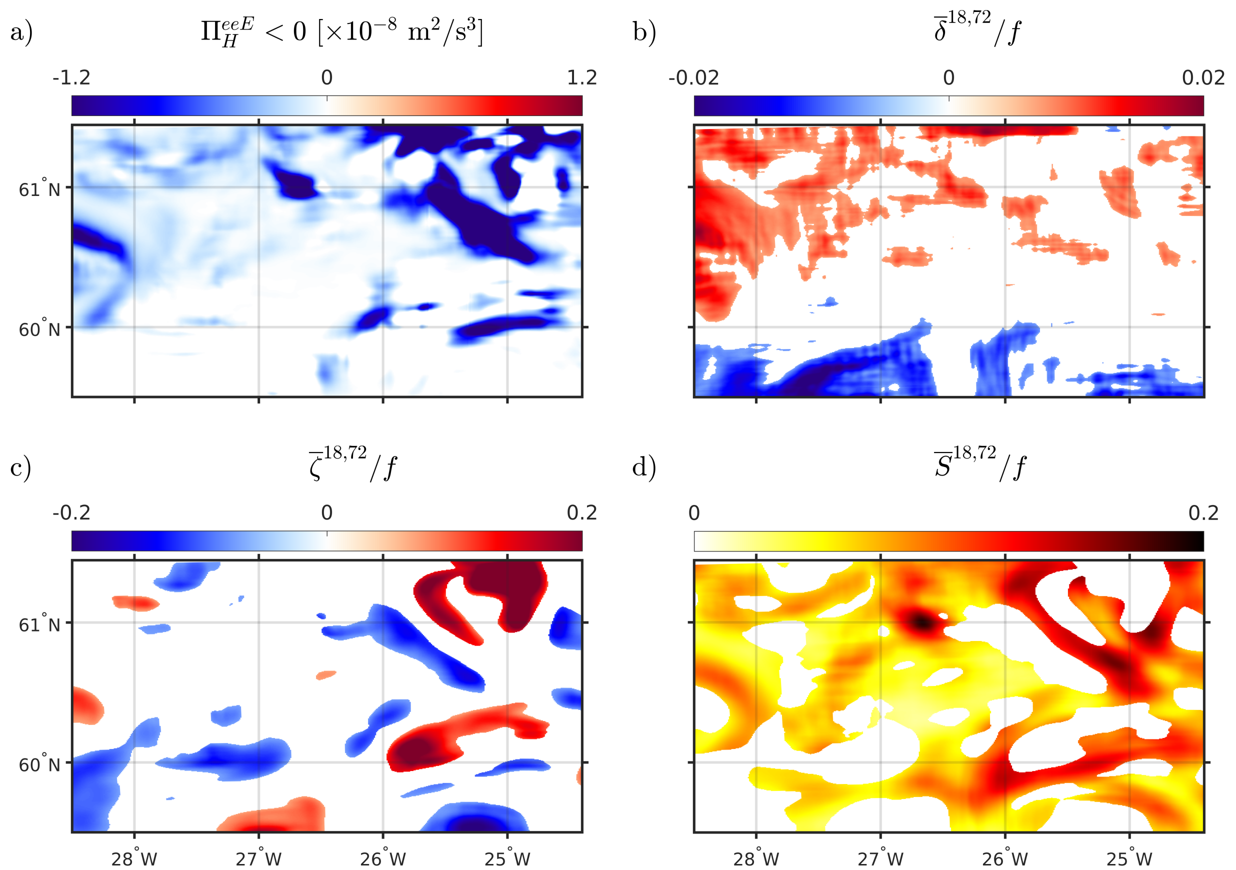


FIG. 12. Same as Fig. 11 during summer but with the eddy field comprising $\Pi_H^{eeE}$ computed with 72 hour low-passed fields and across $\ell = \lambda/2.4 = 18$km. The $\delta/f$, $\zeta/f$, and $S/f$ fields are smoothed accordingly. The vorticity field is only plotted where $\zeta^2 > S^2$ and the strain field is only plotted where $S^2 > \zeta^2$. $\Pi_H^{eeE}$ is only plotted where it is larger than the mean, and only negative fluxes are shown. $\delta/f$, $\zeta/f$, and $S/f$ are only plotted where they are larger than 0.01. Note that the subdomain chosen is larger than in Fig. 11. The corresponding correlation coefficients are displayed in Table 2.

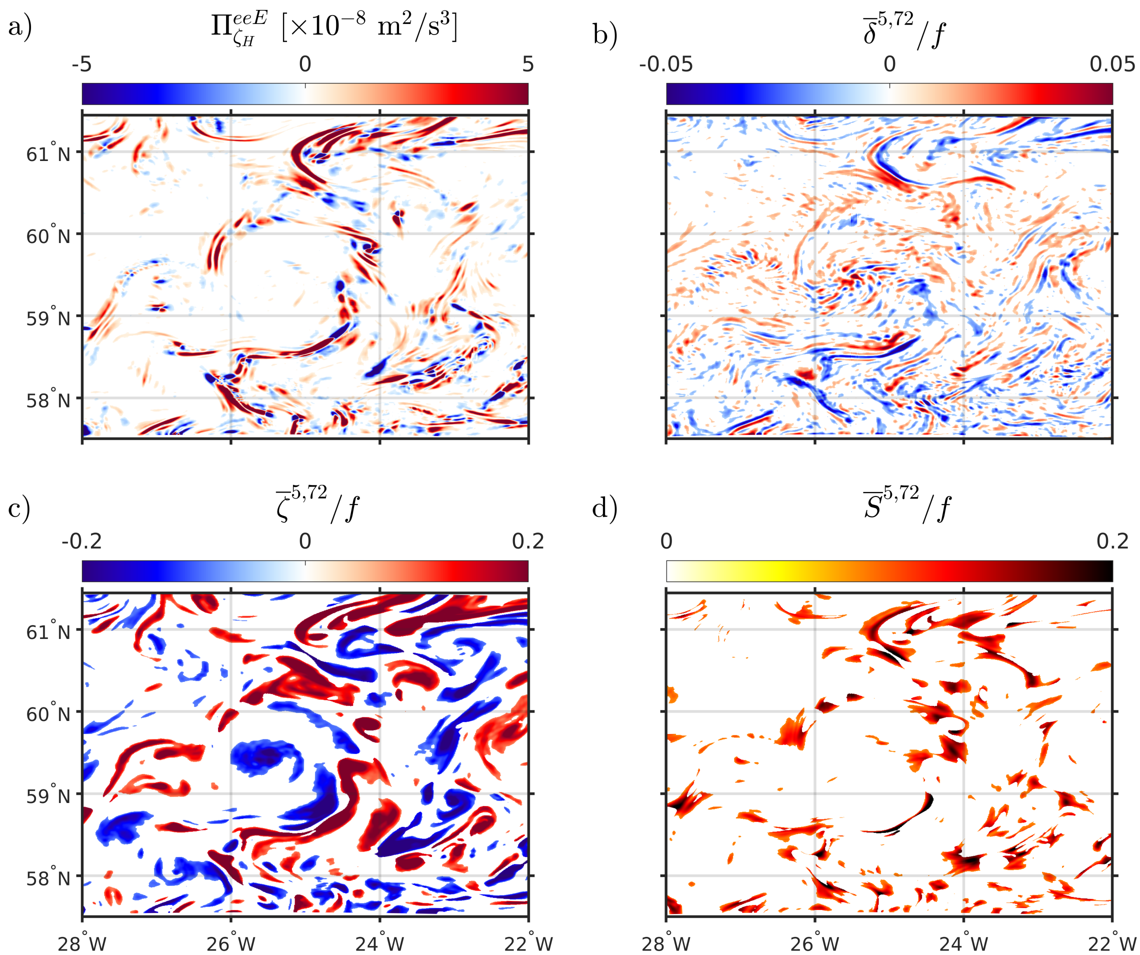


FIG. 13. Representative snapshots of a) horizontal cross-scale enstrophy fluxes and b-d) dynamical flow fields during summer, computed at 2 m depth. The eddy field comprising $\Pi^{eeE}_{\zeta_H}$ (panel a) is computed with 72 hour low-passed fields and fluxes are computed across $\ell = \lambda/2.4 = 5$km. The corresponding $\delta/f$ (panel b), $\zeta/f$ (panel c), and $S/f$ (panel d) fields are spatially and temporally low-passed accordingly; e.g., $\overline{\delta}^{5,72}$ denotes the 72 hour temporally low-passed and 5 km spatially low-passed horizontal divergence field. The vorticity field is only plotted where $\zeta^2 > S^2$ and the strain field is only plotted where $S^2 > \zeta^2$. $\Pi^{eeE}_{\zeta_H}$ is only plotted where it is larger than the mean and $\delta/f$, $\zeta/f$, and $S/f$ are only plotted where they are larger than 0.07. The corresponding correlation coefficients are displayed in Table 3.

*Acknowledgments.* R.B, K.S, and J.C.M were supported by ONR-N000141812697. R.B was further supported by NSF Grant OCE-1851397 and Israeli Science Foundation grant 1736/18. Computation of model simulations and most of the scale-to-scale analysis used here was performed on Extreme Science and Engineering Discovery Environment (XSEDE) clusters (Towns et al. 2014).

*Data availability statement.* The 2 km and 500 m ROMS- based North Atlantic simulations used in this study are not publicly archived but can be made available through direct requests to the corresponding author. The CFSR reanalysis product (Saha et al. 2014; Dee et al. 2014) used to force the ROMS simulation can be found at Saha et al. (2010). The TPXO product (Egbert et al. 1994; Egbert and Erofeeva 2002) used for boundary conditions in the *hf* solution can be found at https://www.tpxo.net/global.

# APPENDIX

## The coarse-grained enstrophy equations

We begin with the vertical component of the vorticity equation $\zeta = \hat{k}\cdot\nabla\times\boldsymbol{u} = -\epsilon_{ik}\partial_k u_i$

$$\frac{D}{Dt}\zeta = -\delta\zeta - f\delta \underbrace{-\epsilon_{ik}\Gamma_k\partial_i w}_{A_{v_\zeta}} + \mathcal{S} - \mathcal{D}, \tag{A1}$$

where $D/Dt = \partial_t + u_j\partial_j$; $\boldsymbol{u} = u_j = (u_1, u_2, u_3) = (u, v, w)$; $\delta = u_x + v_y = \partial_i u_i$; $f$ is the Coriolis frequency (assuming an f-plane for simplicity); $i,k = 1,2$; $j = 1-3$; $\Gamma_k = (u_z, v_z)$; $\epsilon_{ik}$ is the Levi-Civita symbol; $\mathcal{S} = -\epsilon_{ik}\partial_k s_i$ and $\mathcal{D} = -\epsilon_{ik}\partial_k d_i$ are external vorticity sources and sinks associated with any momentum sources and sinks $s_i$ and $d_i$; $x_j = (x_1, x_2, x_3) = (x, y, z)$; subscripts denote derivatives; and repeated indices are summed over.

To derive the coarse-grained enstorphy ($\overline{Z} = \overline{\zeta}^2/2$) evolution equation we apply a low-passed filter of width $\ell$, denoted by $\overline{()}$, to Eq. (A1), multiply by $\overline{\zeta}$, and obtain

$$\frac{\overline{D}}{Dt}\overline{Z} + \frac{\partial}{\partial x_j}(\overline{\zeta}\mathcal{Z}_j) = -\Pi_\zeta(x_j,t,\ell) - \overline{\delta\zeta}\,\overline{\zeta} - f\overline{\delta}\,\overline{\zeta} + \overline{A}_{v_\zeta}\overline{\zeta} + \overline{\zeta}\,\overline{\mathcal{S}} - \overline{\zeta}\,\overline{\mathcal{D}}, \tag{A2}$$

where $\overline{D}/Dt = \partial_t + \overline{u}_j \partial_j$; $\mathcal{Z}_j = \overline{u_j \zeta} - \overline{u_j}\,\overline{\zeta}$; and $\Pi_\zeta = -\mathcal{Z}_j \partial\overline{\zeta}/\partial x_j$ denotes the coarse-grained fluxes. To simplify the notation we drop the superscript $\ell$ from the low-pass filtering operation here, although we keep it in Eq. (2).

The corresponding small-scale enstrophy ($Z' = \overline{\zeta^2}/2 - \overline{\zeta}^2/2$) equation is derived by multiplying Eq. (A1) by $\zeta$, applying the filtering operator, and then subtracting Eq. (A2) from it, leading to

$$\frac{\overline{D}}{Dt}Z' + \frac{\partial}{\partial x_j}(\tau_j^Z - \overline{\zeta}\mathcal{Z}_j) = \Pi_\zeta(x_j, t, \ell) - \tau^{\delta\zeta} - \tau^{f\zeta} + \tau^{A_v\zeta} + \tau^{S\zeta} - \tau^{D\zeta}, \tag{A3}$$

where

$$\begin{aligned} \tau_j^Z = \overline{u_j\zeta^2/2} - \overline{u}_j\,\overline{\zeta^2/2}, \quad \tau^{\delta\zeta} = \overline{\delta\zeta^2} - \overline{\delta\zeta}\,\overline{\zeta}, \quad \tau^{f\zeta} = f\overline{\delta\zeta} - f\overline{\delta}\,\overline{\zeta}, \\ \tau^{A_v\zeta} = \overline{A_v\zeta} - \overline{A_v}\,\overline{\zeta}, \quad \tau^{S\zeta} = \overline{\mathcal{S}\zeta} - \overline{\mathcal{S}}\,\overline{\zeta}, \quad \tau^{D\zeta} = \overline{\mathcal{D}\zeta} - \overline{\mathcal{D}}\,\overline{\zeta}. \end{aligned} \tag{A4}$$

Because $\Pi_\zeta$ appears with opposite signs in Eqs. (A2) and (A3) it denotes energy fluxes to scales smaller than (larger than) $\ell$ when positive (negative). As discussed in Eyink (2005) this definition of $\Pi_\zeta$ is the only one that is Galilean invariant.

## References


Aluie, H., M. Hecht, and G. K. Vallis, 2018: Mapping the energy cascade in the North Atlantic ocean: The coarse-graining approach. *Journal of Physical Oceanography*, **48 (2)**, 225–244.

Balwada, D., J.-H. Xie, R. Marino, and F. Feraco, 2022: Direct observational evidence of an oceanic dual kinetic energy cascade and its seasonality. *Science Advances*, **8 (41)**, eabq2566.

Barkan, R., M. J. Molemaker, K. Srinivasan, J. C. McWilliams, and E. A. D'Asaro, 2019: The role of horizontal divergence in submesoscale frontogenesis. *Journal of Physical Oceanography*, **49 (6)**, 1593–1618.

Barkan, R., K. Srinivasan, L. Yang, J. C. McWilliams, J. Gula, and C. Vic, 2021: Oceanic mesoscale eddy depletion catalyzed by internal waves. *Geophysical Research Letters*, **48 (18)**, e2021GL094 376.

Barkan, R., K. B. Winters, and J. C. McWilliams, 2017: Stimulated imbalance and the enhancement of eddy kinetic energy dissipation by internal waves. *J. Phys. Oceanogr.*, **47**, 181–198.

Callies, J., R. Barkan, and A. N. Garabato, 2020: Time scales of submesoscale flow inferred from a mooring array. *Journal of Physical Oceanography*, **50 (4)**, 1065–1086.

Callies, J., R. Ferrari, J. M. Klymak, and J. Gula, 2015: Seasonality in submesoscale turbulence. *Nature Comm.*, **6**.

Capet, X., J. C. McWilliams, M. J. Molemaker, and A. F. Shchepetkin, 2008a: Mesoscale to submesoscale transition in the California Current System. Part ii: Frontal processes. *J. Phys. Oceangr.*, **38**, 44–64.

Capet, X., J. C. McWilliams, M. J. Molemaker, and A. F. Shchepetkin, 2008b: Mesoscale to submesoscale transition in the California Current System. Part iii: Energy balance and flux. *J. Phys. Oceangr.*, **38**, 2256–2269.

Chaigneau, A., O. Pizarro, and W. Rojas, 2008: Global climatology of near-inertial current characteristics from lagrangian observations. *Geophys. Res. Letts.*, **35**.

Charney, J. G., 1971: Geostrophic turbulence. *Journal of the Atmospheric Sciences*, **28 (6)**, 1087–1095.

Cox, M. R., H. A. Kafiabad, and J. Vanneste, 2023: Inertia-gravity-wave diffusion by geostrophic turbulence: the impact of flow time dependence. *Journal of Fluid Mechanics*, **958**, A21.

D'Asaro, E. A., and Coauthors, 2018: Ocean convergence and the dispersion of flotsam. *Proceedings of the National Academy of Sciences*, **115 (6)**, 1162–1167.

Dee, D., M. Balmaseda, G. Balsamo, R. Engelen, A. Simmons, and J.-N. Thépaut, 2014: Toward a consistent reanalysis of the climate system. *Bulletin of the American Meteorological Society*, **95 (8)**, 1235–1248.

Delpech, A., R. Barkan, K. Srinivasan, J. C. McWilliams, B. K. Arbic, Q. Siyanbola, Oladeji, and M. C. Buijsman, 2023: Eddy - internal wave interactions and their contributions to cross-scale energy fluxes: a case study in the california current. *Journal of Physical Oceanography*, submitted.

Dong, W., O. Bühler, and K. S. Smith, 2020: Frequency diffusion of waves by unsteady flows. *Journal of Fluid Mechanics*, **905**, R3.

Dong, W., O. Bühler, and K. S. Smith, 2023: Geostrophic eddies spread near-inertial wave energy to high frequencies. *Journal of Physical Oceanography*, **53 (5)**, 1311–1322.

Eden, C., F. Pollmann, and D. Olbers, 2019: Numerical evaluation of energy transfers in internal gravity wave spectra of the ocean. *Journal of Physical Oceanography*, **49 (3)**, 737–749.

Egbert, G. D., A. F. Bennett, and M. G. Foreman, 1994: Topex/poseidon tides estimated using a global inverse model. *Journal of Geophysical Research: Oceans*, **99 (C12)**, 24 821–24 852.

Egbert, G. D., and S. Y. Erofeeva, 2002: Efficient inverse modeling of barotropic ocean tides. *Journal of Atmospheric and Oceanic technology*, **19 (2)**, 183–204.

Eyink, G. L., 2005: Locality of turbulent cascades. *Physica D: Nonlinear Phenomena*, **207 (1-2)**, 91–116.

Fox-Kemper, B., R. Ferrari, and R. Hallberg, 2008: Parameterization of mixed layer eddies. Part I: Theory and diagnosis. *J. Phys. Oceangr.*, **38**, 1145–1165.

Fratantoni, D. M., 2001: North Atlantic surface circulation during the 1990's observed with satellite-tracked drifters. *J. Geophys. Res.: Oceans*, **106**, 22 067–22 093.

Garabato, A. C. N., X. Yu, J. Callies, R. Barkan, K. L. Polzin, E. E. Frajka-Williams, C. E. Buckingham, and S. M. Griffies, 2022: Kinetic energy transfers between mesoscale and submesoscale motions in the open ocean's upper layers. *Journal of Physical Oceanography*, **52 (1)**, 75–97.

Garrett, C. J. R., and W. H. Munk, 1972: Space-time scales of internal waves. *Geophys. Fluid Dynamics.*, **2**, 225–264.

Germano, M., 1992: Turbulence- the filtering approach. *Journal of Fluid Mechanics*, **238 (1)**, 325–336.

Hua, B. L., J. C. McWILLIAMS, and P. Klein, 1998: Lagrangian accelerations in geostrophic turbulence. *Journal of Fluid Mechanics*, **366**, 87–108.

Jakobsen, P. K., M. H. Ribergaard, D. Quadfasel, T. Schmith, and C. W. Hughes, 2003: Near-surface circulation in the northern North Atlantic as inferred from lagrangian drifters: Variability from the mesoscale to interannual. *J. Geophys. Res.: Oceans*, **108**.

Kafiabad, H. A., M. A. Savva, and J. Vanneste, 2019: Diffusion of inertia-gravity waves by geostrophic turbulence. *Journal of Fluid Mechanics*, **869**, R7.

Kar, S., and R. Barkan, 2023: Kinetic energy exchanges between a two-dimensional front and internal waves. *Journal of Physical Oceanography*, in press.

Lvov, Y. V., K. L. Polzin, and N. Yokoyama, 2012: Resonant and near-resonant internal wave interactions. *Journal of Physical Oceanography*, **42 (5)**, 669–691.

MacKinnon, J. A., and Coauthors, 2017: Climate process team on internal wave–driven ocean mixing. *Bulletin of the American Meteorological Society*, **98 (11)**, 2429–2454.

McComas, C. H., and F. P. Bretherton, 1977: Resonant interaction of oceanic internal waves. *Journal of Geophysical Research*, **82 (9)**, 1397–1412.

McWilliams, J. C., 2016: Submesoscale currents in the ocean. *Proc. R. Soc. A*, The Royal Society, 20160117.

Okubo, A., 1970: Horizontal dispersion of floatable particles in the vicinity of velocity singularities such as convergences. *Deep sea research and oceanographic abstracts*, Elsevier, Vol. 17, 445–454.

Rama, J., C. J. Shakespeare, and A. M. Hogg, 2022: Importance of background vorticity effect and doppler shift in defining near-inertial internal waves. *Geophysical Research Letters*, **49 (22)**, e2022GL099 498.

Rocha, C. B., G. L. Wagner, and W. R. Young, 2018: Stimulated generation: Extraction of energy from balanced flow by near-inertial waves. *Journal of Fluid Mechanics*, **847**.

Saha, S., and Coauthors, 2010: Ncep climate forecast system reanalysis (cfsr) selected hourly time-series products, january 1979 to december 2010. Research Data Archive at the National Center for Atmospheric Research, Computational and Information Systems Laboratory, Boulder CO, URL https://doi.org/10.5065/D6513W89.

Saha, S., and Coauthors, 2014: The ncep climate forecast system version 2. *Journal of climate*, **27 (6)**, 2185–2208.

Salmon, R., 1980: Baroclinic instability and geostrophic turbulence. *Geophys. Astrophys. Fluid Dyn.*, **15**, 165–211.

Savva, M. A., H. A. Kafiabad, and J. Vanneste, 2021: Inertia-gravity-wave scattering by three-dimensional geostrophic turbulence. *Journal of Fluid Mechanics*, **916**, A6.

Schubert, R., J. Gula, R. J. Greatbatch, B. Baschek, and A. Biastoch, 2020: The submesoscale kinetic energy cascade: Mesoscale absorption of submesoscale mixed layer eddies and frontal downscale fluxes. *Journal of Physical Oceanography*, **50 (9)**, 2573–2589.

Shaham, M., and R. Barkan, 2023: Spectral flux decomposition in turbulent channel flow with near-inertial waves. *Journal of Advances in Modeling Earth Systems*, submitted.

Shakespeare, C. J., A. H. Gibson, A. M. Hogg, S. D. Bachman, S. R. Keating, and N. Velzeboer, 2021: A new open source implementation of lagrangian filtering: A method to identify internal waves in high-resolution simulations. *Journal of Advances in Modeling Earth Systems*, **13 (10)**, e2021MS002 616.

Shchepetkin, A. F., and J. C. McWilliams, 2005: The Regional Oceanic Modeling System: A split-explicit, free-surface, topography-following-coordinate oceanic model. *Ocean Modelling*, **9**, 347–404.

Srinivasan, K., R. Barkan, and J. C. McWilliams, 2023: A forward energy flux at submesoscales driven by frontogenesis. *Journal of Physical Oceanography*, **53 (1)**, 287–305.

Taylor, S., and D. Straub, 2016: Forced near-inertial motion and dissipation of low-frequency kinetic energy in a wind-driven channel flow. *J. Phys. Oceanogr.*, **46 (1)**, 79–93.

Taylor, S., and D. Straub, 2020: Effects of adding forced near-inertial motion to a wind-driven channel flow. *Journal of Physical Oceanography*, **50 (10)**, 2983–2996.

Thomas, J., and D. Daniel, 2020: Turbulent exchanges between near-inertial waves and balanced flows. *Journal of Fluid Mechanics*, **902 (LA-UR-19-32700)**.

Thomas, J., and D. Daniel, 2021: Forward flux and enhanced dissipation of geostrophic balanced energy. *Journal of Fluid Mechanics*, **911**.

Thomas, L., L. Rainville, O. Asselin, W. R. Young, J. Girton, C. B. Whalen, L. Centurioni, and V. Hormann, 2020: Direct observations of near-inertial wave $\zeta$-refraction in a dipole vortex. *Geophysical Research Letters*, **47 (21)**, e2020GL090 375.

Thomas, L. N., 2012: On the effects of frontogenetic strain on symmetric instability and inertia-gravity waves. *J. Fluid Mech.*, **711**, 620–640.

Thomas, L. N., E. D. Skyllingstad, L. Rainville, V. Hormann, L. Centurioni, J. N. Moum, O. Asselin, and C. M. Lee, 2023: Damping of inertial motions through the radiation of near-inertial waves in a dipole vortex in the iceland basin. *Journal of Physical Oceanography*.

Thomas, L. N., A. Tandon, and A. Mahadevan, 2008: Submesoscale processes and dynamics. *Ocean Modeling in and Eddying Regime*, M. Hecht, and H. Hasumi, Eds., Vol. 177, AGU Geophysical Monograph Series, 17–38.

Torres, H. S., and Coauthors, 2022: Separating energetic internal gravity waves and small-scale frontal dynamics. *Geophysical Research Letters*, **49 (6)**, e2021GL096 249.

Towns, J., and Coauthors, 2014: Xsede: accelerating scientific discovery. *Computing in science & engineering*, **16 (5)**, 62–74.

Vanneste, J., 2013: Balance and spontaneous wave generation in geophysical flows. *Annual Review of Fluid Mechanics*, **45**, 147–172.

Wagner, G., and W. Young, 2016: A three-component model for the coupled evolution of near-inertial waves, quasi-geostrophic flow and the near-inertial second harmonic. *J. Fluid Mech.*, **802**, 806–837.

Wang, C., Z. Liu, and H. Lin, 2023: On dynamical decomposition of multiscale oceanic motions. *Journal of Advances in Modeling Earth Systems*, **15 (3)**, e2022MS003 556.

Weiss, J., 1991: The dynamics of enstrophy transfer in two-dimensional hydrodynamics. *Physica D: Nonlinear Phenomena*, **48 (2-3)**, 273–294.

Whitt, D. B., and L. N. Thomas, 2013: Near-inertial waves in strongly baroclinic currents. *J. Phys. Oceanogr.*, **43**, 706–725.

Whitt, D. B., and L. N. Thomas, 2015: Resonant generation and energetics of wind-forced near-inertial motions in a geostrophic flow. *J. Phys. Oceanogr.*, **45 (1)**, 181–208.

Wunsch, C., and R. Ferrari, 2004: Vertical mixing, energy, and the general circulation of the oceans. *Ann. Rev. Fluid Mech.*, **36**, 281–314.

Xie, J.-H., 2020: Downscale transfer of quasigeostrophic energy catalyzed by near-inertial waves. *Journal of Fluid Mechanics*, **904**, A40.

Xie, J.-H., and J. Vanneste, 2015: A generalised-lagrangian-mean model of the interactions between near-inertial waves and mean flow. *Journal of Fluid Mechanics*, **774**, 143–169.

Yang, L., R. Barkan, K. Srinivasan, J. C. McWilliams, C. J. Shakespear, and A. H. Gibson, 2023: Oceanic eddies induce a rapid formation of an internal wave continuum. *Communications Earth and Environment*, under review.

Zhang, L.-F., and J.-H. Xie, 2023: The catalytic effect of near-inertial waves on-plane zonal jets. *Journal of Fluid Mechanics*, **962**, A33.